The CARMENES search for exoplanets around M dwarfs: guaranteed time observations Data Release 1 (2016-2020)

Ribas, I.; Reiners, A.; Zechmeister, M.; Caballero, J.A.; Morales, J.C.; Sabotta, S.; ... ;
Zapatero Osorio, M.R.

Astronomy & Astrophysics

The CARMENES search for exoplanets around M dwarfs

Guaranteed time observations Data Release 1 (2016-2020)[⋆]

I. Ribas[1,2] , A. Reiners[3] , M. Zechmeister[3], J. A. Caballero[4,5] , J. C. Morales[1,2] , S. Sabotta[5,6], D. Baroch[1,2] ,
P. J. Amado[7] , A. Quirrenbach[5], M. Abril[7], J. Aceituno[8,7], G. Anglada-Escudé[1,2], M. Azzaro[8] , D. Barrado[4] ,
V. J. S. Béjar[9,10] , D. Benítez de Haro[8], G. Bergond[8] , P. Bluhm[5] , R. Calvo Ortega[7] , C. Cardona Guillén[9,10] ,
P. Chaturvedi[6], C. Cifuentes[4] , J. Colomé[1,2] , D. Cont[3] , M. Cortés-Contreras[4] , S. Czesla[6,11] , E. Díez-Alonso[12,13] ,
S. Dreizler[3] , C. Duque-Arribas[13] , N. Espinoza[14,15,16], M. Fernández[7], B. Fuhrmeister[11], D. Galadí-Enríquez[8],
A. García-López[17,4] , E. González-Álvarez[18], J. I. González Hernández[9,10] , E. W. Guenther[6], E. de Guindos[8] ,
A. P. Hatzes[6], Th. Henning[16], E. Herrero[1,2] , D. Hintz[19,11] , Á. L. Huelmo[7], S. V. Jeffers[20,3] , E. N. Johnson[3,20] ,
E. de Juan[8] , A. Kaminski[5], J. Kemmer[5] , J. Khaimova[3], S. Khalafinejad[5,16], D. Kossakowski[16] , M. Kürster[16] ,
F. Labarga[13], M. Lafarga[21,1,2] , S. Lalitha[22,11] , M. Lampón[7] , J. Lillo-Box[4] , N. Lodieu[9,10] ,
M. J. López González[7], M. López-Puertas[7], R. Luque[23,9,10,7] , H. Magán[7,8] , L. Mancini[24,25,16] ,
E. Marfil[9,10,4,13] , E. L. Martín[9,10,26] , S. Martín-Ruiz[7], K. Molaverdikhani[27,28,5,16] , D. Montes[13] ,
E. Nagel[11,6] , L. Nortmann[3,9,10] , G. Nowak[9,10] , E. Pallé[9,10] , V. M. Passegger[9,10,11,29] , A. Pavlov[16],
S. Pedraz[8] , V. Perdelwitz[30,11] , M. Perger[1,2] , A. Ramón-Ballesta[7] , S. Reffert[5] , D. Revilla[7,13],
E. Rodríguez[7] , C. Rodríguez-López[7] , S. Sadegi[5], M. Á. Sánchez Carrasco[7] , A. Sánchez-López[31,7] ,
J. Sanz-Forcada[4] , S. Schäfer[3] , M. Schlecker[32,16] , J. H. M. M. Schmitt[11], P. Schöfer[7,3] , A. Schweitzer[11] ,
W. Seifert[5], Y. Shan[33,3] , S. L. Skrzypinski[13], E. Solano[4] , O. Stahl[5], M. Stangret[34,9,10] , S. Stock[5] , J. Stürmer[5,23],
H. M. Tabernero[18] , L. Tal-Or[35,3] , T. Trifonov[16,36], S. Vanaverbeke[37,38,39] ,
F. Yan[40,3] , and M. R. Zapatero Osorio[18]

(Affiliations can be found after the references)

ABSTRACT

Context. The CARMENES instrument, installed at the 3.5 m telescope of the Calar Alto Observatory in Almería, Spain, was conceived to deliver high-accuracy radial velocity (RV) measurements with long-term stability to search for temperate rocky planets around a sample of nearby cool stars. Moreover, the broad wavelength coverage was designed to provide a range of stellar activity indicators to assess the nature of potential RV signals and to provide valuable spectral information to help characterise the stellar targets.

Aims. We describe the CARMENES guaranteed time observations (GTO), spanning from 2016 to 2020, during which 19 633 spectra for a sample of 362 targets were collected. We present the CARMENES Data Release 1 (DR1), which makes public all observations obtained during the GTO of the CARMENES survey.

Methods. The CARMENES survey target selection was aimed at minimising biases, and about 70% of all known M dwarfs within 10 pc and accessible from Calar Alto were included. The data were pipeline-processed, and high-level data products, including 18 642 precise RVs for 345 targets, were derived. Time series data of spectroscopic activity indicators were also obtained.

Results. We discuss the characteristics of the CARMENES data, the statistical properties of the stellar sample, and the spectroscopic measurements. We show examples of the use of CARMENES data and provide a contextual view of the exoplanet population revealed by the survey, including 33 new planets, 17 re-analysed planets, and 26 confirmed planets from transiting candidate follow-up. A subsample of 238 targets was used to derive updated planet occurrence rates, yielding an overall average of 1.44 ± 0.20 planets with $1\,M_\oplus < M_{\rm pl} \sin i < 1000\,M_\oplus$ and 1 day $< P_{\rm orb} <$ 1000 days per star, and indicating that nearly every M dwarf hosts at least one planet. All the DR1 raw data, pipeline-processed data, and high-level data products are publicly available online.

Conclusions. CARMENES data have proven very useful for identifying and measuring planetary companions. They are also suitable for a variety of additional applications, such as the determination of stellar fundamental and atmospheric properties, the characterisation of stellar activity, and the study of exoplanet atmospheres.

Key words. techniques: spectroscopic – astronomical databases: miscellaneous – planetary systems – stars: late-type – solar neighborhood

1. Introduction

M-type dwarfs provide some advantages with respect to Sun-like stars in the search for exoplanets, particularly those with low

masses. Their relatively small sizes and masses result in stronger planetary signals. Furthermore, their low intrinsic luminosities imply that temperate planets orbiting within their liquid-water habitable zone have shorter orbital periods, of the order of tens of days (Kopparapu et al. 2013). In addition, they constitute an abundant stellar population, comprising the majority of stars (78.5%) in the solar neighbourhood (Reylé et al. 2021). The main

---

drawbacks of M dwarfs as targets for exoplanet searches are their intrinsic faintness and the fact that a relatively large fraction of them show magnetic activity phenomena, especially the later spectral types (Reiners et al. 2012). A number of efforts have successfully exploited the so-called M-dwarf opportunity for planet detection over the past few decades (e.g. Delfosse et al. 1999; Endl et al. 2003; Wright et al. 2004; Bonfils et al. 2005; Nutzman & Charbonneau 2008; Zechmeister et al. 2009; Johnson et al. 2010; Ricker et al. 2015; Affer et al. 2016; Seifahrt et al. 2018; Bayliss et al. 2018).

The CARMENES[1] instrument and survey were specifically conceived to search for temperate rocky planets around a sample of nearby cool stars (Quirrenbach et al. 2014). The spectrograph was designed to provide high-accuracy radial velocity (RV) measurements with long-term stability in a broad wavelength interval where M-dwarf stars have the peak of their spectral energy distribution. Moreover, such wide coverage provides a range of stellar activity indicators to assess the nature of potential RV signals as well as valuable spectral information that can be used to characterise the stellar targets.

The CARMENES instrument is installed at the 3.5 m telescope of the Calar Alto Observatory in Almería, Spain (37°13′25″N, 2°32′46″W). It provides nearly continuous wavelength coverage from 520 nm to 1710 nm from its two channels: the visual channel (VIS), with a spectral resolution of $R = 94\,600$, covers the range $\lambda = 520$–960 nm, while the near-infrared channel (NIR) yields a resolution of $R = 80\,400$ within a wavelength interval $\lambda = 960$–1710 nm (Quirrenbach et al. 2016). Both channels are coupled to the telescope by optical fibres, with a projection of $1″5$ on the sky.

A sample of about 350 M dwarfs across all M spectral subtypes comprises the targets of the main survey. A total of 750 useful nights were reserved as guaranteed time observations (GTO) for the CARMENES consortium, and these ran for 5 yr, from 1 January 2016 to 31 December 2020.

The present publication accompanies the release of the observations acquired with the CARMENES VIS channel over the course of the RV survey within the GTO programme, which we have dubbed the CARMENES Data Release 1 (DR1). This includes raw data, calibrated spectra, and high-level data products, such as RVs and spectroscopic indicators. The paper is structured as follows. Section 2 describes the design and execution of the CARMENES survey. In Sect. 3, we present the CARMENES GTO target sample and provide a description of its statistical distribution. Section 4 describes the observations collected within the GTO and the processing data flow from raw frames to calibrated RVs and ancillary data products. In Sect. 5, we discuss the properties of the CARMENES DR1 regarding internal and external precision, we provide information regarding the presence of periodic signals in the data, and we present and discuss the sample of exoplanets in the surveyed targets. Furthermore, we present revised planet occurrence rates considering all publicly released data. Finally, Sect. 6 provides the summary and conclusions of the work.

2. The CARMENES survey

The initial goal of the GTO survey was to collect approximately 70 spectra for each of the foreseen 300 targets (Garcia-Piquer et al. 2017), which would have yielded a grand total of ~21 000

spectra. During the survey, we identified a number of targets with high-amplitude RV variations (RV scatter $>10\,\mathrm{m\,s^{-1}}$ and $v \sin i > 2\,\mathrm{km\,s^{-1}}$), which we classified as RV-loud (Tal-Or et al. 2018). For each of them, we obtained about 11 observations and monitoring was subsequently discontinued. A similar approach was followed for spectroscopic binaries, for which we acquired a number of measurements just enough to derive reliable orbital solutions (Baroch et al. 2018, 2021). For some of the binaries with the longest periods, however, monitoring at very low cadence has been extended over time to constrain better the orbital and physical parameters of the components.

Despite the discontinued targets, sometime into the survey it was realised that reaching 70 observations per star would not be possible, mostly because of the large number of measurements needed to characterise newly discovered exoplanets as a consequence of the measured astrophysical jitter and also because of the telescope and instrument overhead times being somewhat longer than initially considered. Furthermore, with the launch of the Transiting Exoplanet Survey Satellite (TESS) mission in 2018 (Ricker et al. 2015), the CARMENES Consortium agreed to invest approximately 50 useful GTO nights in following up TESS transiting planet candidates with M-dwarf hosts (CARMENES-TESS follow-up programme). As a consequence of the new circumstances, it was decided that the survey should aim at acquiring a minimum of 50 observations per target, which would yield plenty of planet detections and provide meaningful constraints on planet occurrence rates. At the same time, we redefined the relative priorities of the sample to favour stars of spectral type M4 V and later to exploit optimally the CARMENES capabilities in a relatively unexplored range of stellar host masses. Such a decision implied that the faint end of the M2 V and M3 V targets in the sample would have lower chances of being scheduled because of the employed criteria (Garcia-Piquer et al. 2017).

At the end of the GTO survey in 2020, the minimum number of 50 measurements had not been reached for all surveyed targets. The CARMENES DR1 therefore contains unequal number of observations, with a median of 30 observations per star. However, some of the targets, such as RV standards and stars with suggestive planetary signals, were observed up to a few hundred times. About two thirds of the targets have time series of at least 3 yr, and for almost half of the targets the observations cover at least 4 yr. Only 10% of the targets are observed for less than a year. The cadence is random and non-uniform, not only because of observability but also for scientific reasons and (e.g. priority increased when a planet candidate signal required more detailed sampling). In 2020, a proposal was submitted to the competitive Calar Alto Legacy projects call, and an additional 300 nights were awarded to the CARMENES Consortium to complete the survey during 2021–2023 and, hence, fulfil the goal of attaining at least 50 observations per target.

3. CARMENES GTO sample

The CARMENES GTO sample of M dwarfs is generally composed of the brightest stars of every spectral subtype that are visible from Calar Alto ($\delta > -23°$), as described in Alonso-Floriano et al. (2015). Effectively, this means that about 70% of the full sky is observable by the CARMENES survey. We only excluded stars that are known members of visual binaries at separations closer than 5″. We explicitly did not bias our sample with regard to age, metallicity, or magnetic activity, nor did we exclude stars with planets that were already known. More

---

[1] Calar Alto high-Resolution search for M dwarfs with Exoearths with Near-infrared and optical Échelle Spectrographs; https://carmenes.caha.es

Table 1. Basic properties and number of measurements for the CARMENES DR1 target sample.

Karmn	Star name	N_{AVC}	N_{RVC}	M ($M_\odot$)	R ($R_\odot$)	T_{eff} (K)	P_{rot} (d)	Ref. P_{rot}	Survey	Comments
J00051+457	GJ 2	52	53	0.49	0.49	3773	15.4	DA19	GTO	
J00067−075	GJ 1002	89	91	0.11	0.12	3169			GTO	
J00162+198E	LP 404-062	18	18	0.27	0.28	3329	105.0	DA19	GTO	
J00183+440	GX And	216	223	0.39	0.40	3603	45.0	SM18	GTO	
J00184+440	GQ And	193	196	0.16	0.18	3318			GTO	
J00286−066	GJ 1012	50	53	0.34	0.35	3419			GTO	
J00389+306	Wolf 1056	58	60	0.41	0.41	3551	50.2	DA19	GTO	
J00403+612	2MASS J00402129+6112490	40	41	0.47	0.47	3709			TESS	
J00570+450	G 172-030	16	16	0.33	0.34	3488			GTO	
J01013+613	GJ 47	10	10	0.37	0.37	3564	34.7	SM18	GTO	

Notes. This is a sample list. The full table can be downloaded from CDS.

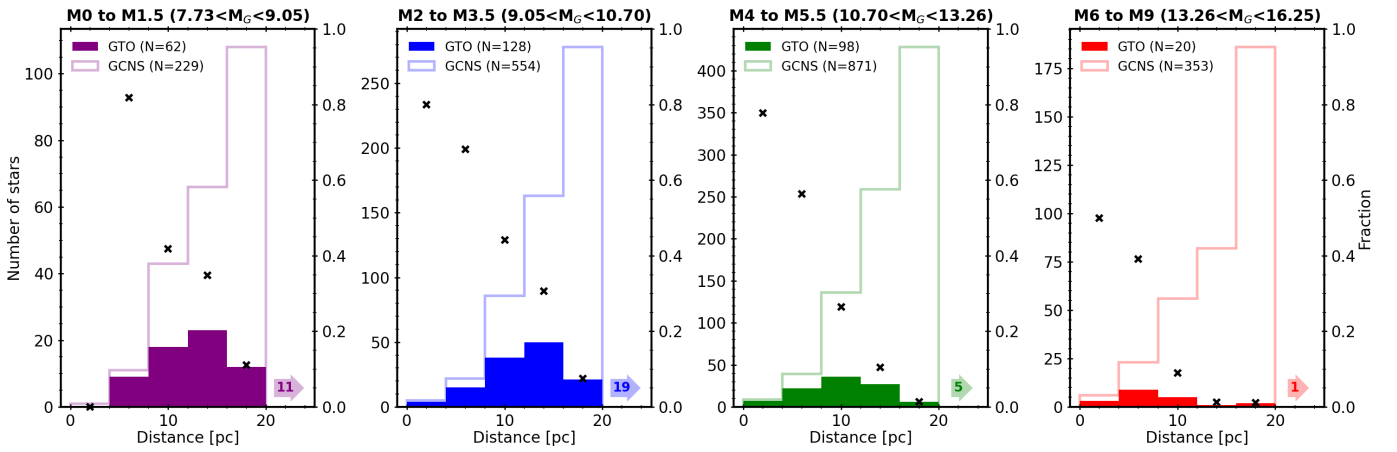**References.** DA19: Díez Alonso et al. (2019), SM18: Suárez Mascareño et al. (2018).

Fig. 1. Distribution of the CARMENES GTO target sample (excluding the SB2 and ST3 systems) as a function of distance ($d < 20$ pc) for different spectral types or absolute *Gaia G*-band intervals. Some stars in the sample are at greater distances, and this number is provided inside the right-pointing arrow. One of the targets at the K–M spectral type boundary has an M_G value below 7.73 mag and is not included; hence, the total number of stars plotted is 344. The distance distribution of the GCNS for the same intervals is also shown, and the ratios between the two are depicted as black crosses with the scale in the right y axis.

information on the selection criteria was provided by Reiners et al. (2018b, hereafter Rei18b) and references therein. The sample described by Rei18b was composed of 324 stars. Throughout the survey we added nine additional targets as a result of supervening circumstances such as new exoplanet announcements, interesting targets (e.g. in the TESS continuous viewing zone), and revised spectroscopic classification. Furthermore, we added 18 targets from the CARMENES-TESS follow-up programme. As opposed to Rei18b, we also included in our current analysis double- and triple-line spectroscopic binaries and triples (SB2 and ST3, respectively) and some visual binaries. We have found 17 of such binaries in the sample, 11 of which are new additions to Rei18b, but six were present there because they had not yet been identified as SB2, ST3, or visual binaries.

Table 1 presents a selection of relevant properties of the 362 targets in the CARMENES GTO sample. The different columns list basic stellar parameters (M, R, T_{eff}), rotation periods (P_{rot}), and the number of measurements in the release, both in the form of pipeline-produced RVs (N_{RVC}) and zero-point-corrected RVs (N_{AVC}). Descriptions of these two data products are provided in Sect. 4. The basic stellar parameters were taken from the latest version of Carmencita, which is the CARMENES input catalogue (Caballero et al. 2016), and from the series of papers on

the characterisation of the CARMENES GTO sample (Alonso-Floriano et al. 2015; Cortés-Contreras et al. 2017; Jeffers et al. 2018; Díez Alonso et al. 2019; Cifuentes et al. 2020; Perdelwitz et al. 2021). In the case of targets where more than one set of lines are visible in the spectra (SB2, ST3, and visual binaries), the basic parameters are not listed (as they are ill-defined) and the column N_{RVC} provides the total number of CARMENES observations released. The penultimate column indicates if the target is part of the blind GTO survey or if it is a TESS exoplanet candidate. An asterisk marks targets already tabulated by Rei18b. We are not discussing here the statistical distribution of the target sample regarding brightness and spectral type. The general properties are equivalent to those in Figs. 2 and 3 of Rei18b, which already comprised most of the sample presented here (>90%).

The volume completeness of the CARMENES GTO sample can be investigated by comparing distance distributions with the *Gaia* Catalogue of Nearby Stars (GCNS; Gaia Collaboration 2021), which is assumed to be complete at the brightness cuts and spectral types of interest. In Fig. 1, we show a collection of histograms as a function of distance out to 20 pc for several spectral type and *Gaia G*-band absolute magnitude (M_G) intervals. To allow for a comparison, spectral types of GCNS stars were estimated from M_G following the corresponding

relationship by Cifuentes et al. (2020). The ratio between the number of stars in the CARMENES sample and the number of known stars in the GCNS is also shown. The ratio, that is, the sample completeness, decreases with M subtype (from 27% for early Ms to 6% for late Ms), as expected due to brightness limitations. The global completeness of the CARMENES sample at 20 pc, including all spectral types, is 15%. If we consider distances to 10 pc, then the ratio of sample stars to known stars exceeds 50% in all intervals except for the latest Ms, where the ratio is 28%. Altogether, the CARMENES GTO sample contains nearly half (48%) of all known M dwarfs within 10 pc of the Sun (Reylé et al. 2021), and about 70% of those accessible from the Calar Alto Observatory. Most nearby M dwarfs that are not in the sample have close companions at less than 5″.

4. Observations

The observations of the CARMENES GTO survey were collected in a signal-to-noise (S/N) limited fashion. That is, using the number of counts from the exposure meter of the NIR channel (c_{EM}) and a calibrated relationship – $S/N \propto \sqrt{c_{EM}}$, – the integration was continued until reaching a S/N of 150 at order 50 (~1200 nm) of the CARMENES NIR channel, or was interrupted after an integration of 1800 s to avoid excessive contamination from cosmic rays and line broadening due to Earth's rotation. According to the calculations by Reiners & Zechmeister (2020), a spectrum with S/N = 150 at 1200 nm for an early- to mid-type M dwarf produces a typical uncertainty of $1\,\mathrm{m\,s^{-1}}$ in RV from photon shot noise, which was the required value for the survey.

A total of 19 633 spectra were acquired as part of the GTO programme. However, a small fraction of them do not have sufficient quality for precise RV work and were not considered in our subsequent analysis. They were flagged by the processing pipeline because of low S/N, high S/N implying saturation risk, contamination by twilight, Moon, or stray light. The total number of spectra yielding useful RV measurements is 19 161. The discarded 472 spectra are still accessible from the Calar Alto archive[2] in raw format but are not part of the CARMENES DR1.

The processing of the data was done automatically with a pipeline, including the reduction of raw frames, the extraction and calibration of spectra, the determination of RVs using a template-matching algorithm, and the calculation of cross-correlation function (CCF) products. Full details on the applied procedure are provided below. The data for SB2 and ST3 targets were only processed up to the extraction and calibration of spectra, and were not analysed to determine precise RVs because our methodology is not suitable when more than one set of stellar lines is present in the spectra. Finally, we provide the full set of data products for 18 642 out of the 19 161 good spectra.

4.1. Processing pipeline

The observations were reduced with the `caracal`[3] pipeline, with the data flow being described by Caballero et al. (2016). The extraction pipeline is based on the `reduce` package of Piskunov & Valenti (2002) but many routines have been revised. In particular, we developed the flat-relative optimal extraction (FOX, Zechmeister et al. 2014) and wavelength calibration scripts, which combine spectra from hollow-cathode lamps (HCLs) and Fabry-Pérot (F-P) étalons (Bauer et al. 2015). The data release in this work is based on `caracal v2.20`.

4.2. Radial velocities

The RVs for the CARMENES DR1 were computed with `serval`[4] (Zechmeister et al. 2018) and `raccoon`[5] (Lafarga et al. 2020). Both software packages were specifically developed for data coming from the CARMENES instrument, although they can process spectroscopic data from other precise RV instruments as well (e.g. Stefánsson et al. 2020; Hoyer et al. 2021; Wang et al. 2022; Turtelboom et al. 2022).

The `serval` code implements a data-driven approach, where both RVs and templates are derived from the observations themselves via a least-squares fitting procedure similar to the Template-Enhanced Radial velocity Re-analysis Application (TERRA; Anglada-Escudé & Butler 2012). The co-adding is performed by cubic B-spline regression. For the barycentric correction, the default option is the Python implementation `barycorrpy`[6] (Wright & Eastman 2014; Kanodia & Wright 2018). The RVs for each spectral order are produced, and the global RV of the spectrum is subsequently computed as a simple weighted mean over the spectral orders. By default, the ten bluest and the ten reddest spectral orders are not used. In those regions, the instrument efficiency decreases. Furthermore, the red end is strongly affected by telluric contamination and dichroic cutoff. For faint late M dwarfs additional blue orders may be omitted because of low S/N. Since the present data release contains the order-wise RVs, a more sophisticated recalculation of RV values (robust means, re-weighting using a posteriori information) employing a detailed chromatic analysis is also possible (e.g. Zechmeister et al. 2019). Finally, corrections for instrumental drift and secular acceleration (Kürster et al. 2003) are applied to the global RV, yielding the so-called RVC (Radial Velocity Corrected) velocities.

The RV error bar is calculated as the weighted mean of the order-wise RVs (see Eq. (15) in Zechmeister et al. 2018) and takes into account photon noise, readout noise, and model mismatch. The last contribution quantifies the difference between the spectrum and the template (caused, for example, by cosmic rays, telluric contamination or detector artefacts), and the excess scatter of the averaged individual orders (caused, for example, by telluric contamination affecting specific orders or a chromatic trend). Thus, formal RV uncertainties are based on the quality of the template fit and not on estimates of any physical effects during observation or calibration (e.g. modal noise). The CARMENES instrument was designed to minimise all such effects (Seifert et al. 2012; Stürmer et al. 2014) but, if anyway present to some extent, they will result in excess noise (instrumental jitter).

A further RV data product is provided, namely AVC (Average Velocity Corrected) velocities. These are obtained from RVCs by correcting for nightly zero points (NZPs; see Sect. 4.4). AVC RVs are not calculated if no instrumental drift value is available. The total error bar of each AVC RV considers the uncertainties of the RVC and the corrections added in quadrature. In addition to RVs, `serval` provides a further set of useful parameters. These include the chromatic index (CRX; a measure of the wavelength dependence of the RVs), the differential line width (dLW), and spectral line indices (e.g. Hα, Ca I,

---

[2] http://caha.sdc.cab.inta-csic.es/calto
[3] CARMENES Reduction And CALibration.

[4] SpEctrum Radial Velocity AnaLyser. https://github.com/mzechmeister/serval. Based on the version committed on 2022-01-26 https://github.com/mzechmeister/serval/tree/a348b4c
[5] Radial velocities and Activity indicators from Cross-COrrelatiON with masks. https://github.com/mlafarga/raccoon
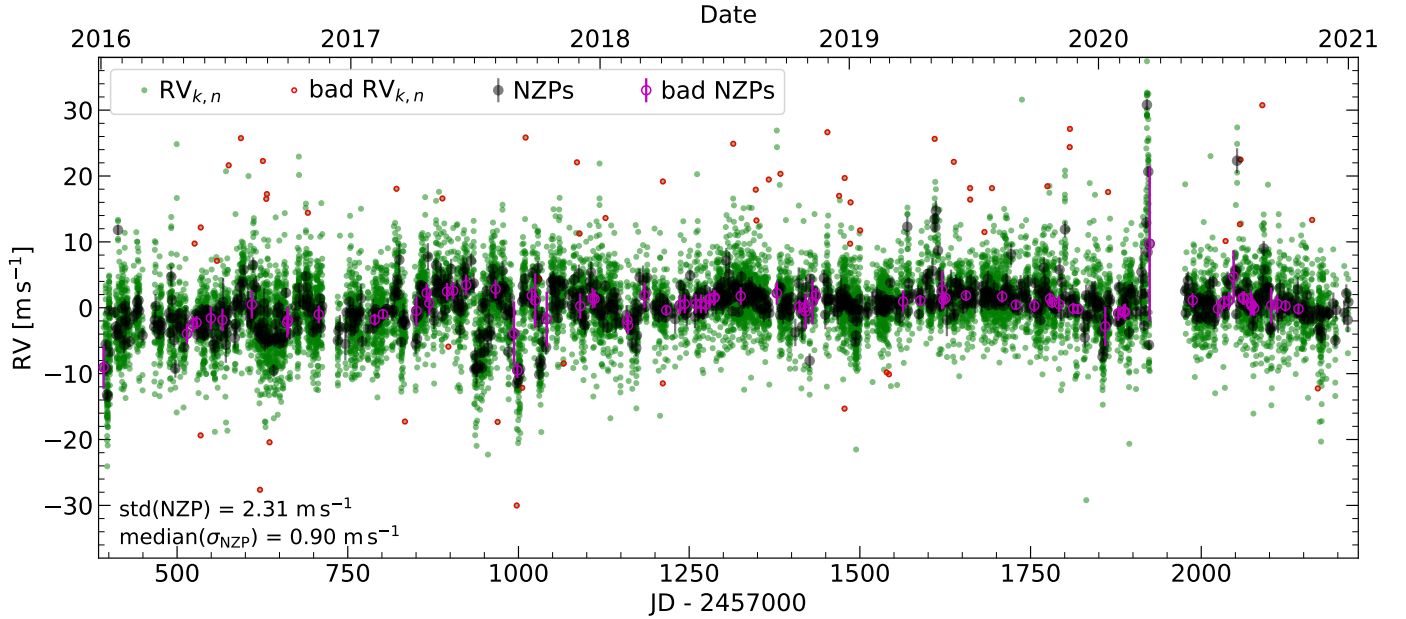[6] https://github.com/shbhuk/barycorrpy

Fig. 2. Nightly zero points (NZPs) of CARMENES VIS. The RVs of all RV constant stars (small green points) are zero-centred. A mean (the NZP, solid black circles) is computed for each night, in which identified outliers (small red points) are omitted. NZPs with fewer than three RV standard observations (open magenta circles) are replaced by a local mean.

Ca II IRT (infrared triplet), and Na I D), which are valuable activity indicators (Fuhrmeister et al. 2019b; Schöfer et al. 2019). A full description of these serval products and their calculation methodologies is provided in Zechmeister et al. (2018).

The raccoon code is based on the CCF concept (Baranne et al. 1996), whereby a weighted binary mask is used to calculate the convolution with each observed spectrum. In our implementation, we derived the mask from the serval template of the target itself. One of the outputs is the RVs, which are known to be less precise than values coming from template matching for M dwarfs (Perger et al. 2017), but still allow for a cross-check with serval. Other relevant CCF parameters produced by raccoon are the contrast (CON), the full width at half maximum (FWHM), and the bisector inverse slope (BIS). These parameters can be regarded as moments of the CCF that carry information on the characteristics of the stellar lines and, therefore, can be used to assess variability coming from astrophysical sources. Further details can be found in Lafarga et al. (2020).

The RVs in the CARMENES DR1 may differ from RVs that have appeared in previous CARMENES publications. This is because serval and raccoon are steadily maintained and new upgrades are continuously made. In addition, all parameters are recalculated when new spectra of a target are considered (i.e. producing a new template) and, thus, slightly different values may result. Finally, the NZP corrections can vary when new data are considered, also impacting on the final velocities. In any case, any differences with published data are generally minor.

4.3. Telluric contamination correction

The Earth atmosphere imprints spectral features from its molecular and atomic components (mostly H_2O and O_2 in the VIS domain), called telluric lines (or tellurics, for short), onto the stellar spectrum. serval handles this contamination by simply masking telluric lines when computing the RVs (during co-adding, telluric lines are strongly down-weighted, and severely contaminated template regions are masked as well during RV

computation). Masking lines is a straightforward and robust first-order approach. The default mask of serval flags regions where the telluric line depth is typically about 5% or greater. Various tests using different thresholds and resulting mask widths showed this value to provide optimal results by trading off wavelength coverage (i.e. RV precision) and systematic effects from telluric contamination. While the telluric mask is static in the detector frame, it moves in the stellar rest frame because of Earth's yearly barycentric motion. To ensure that identical spectral regions are used for RV determination throughout the observing season, an alternative approach would be to mask out the full barycentric velocity range around each telluric feature. However, we preferred not to use such a procedure because it significantly diminishes the available wavelength range and, thus, the amount of RV information.

There may be cases where the residual telluric RV content (due to high airmass or micro-telluric contamination) may still be significant. Such residuals can most likely affect cases where the RV internal precision is very high (e.g. high S/N observations) and where the stellar RV signal is weak (e.g. fast rotators). Residual telluric contamination can result in spurious RV periodicities, mostly yearly signals or their aliases (Damasso et al. 2022). Hence, caution is advised in the interpretation of those typically long-period, low-amplitude signals. Improvements may be made by re-weighting spectral orders, reprocessing with more conservative masks, or employing a more sophisticated telluric modelling scheme (e.g. Nagel 2019).

4.4. Nightly zero points

Although the CARMENES spectrograph is usually wavelength calibrated each afternoon and nightly instrumental drifts are measured with the F-P étalon, stellar RVs from the same night often share common systematic effects, which produce NZP offsets generally of a few $m\,s^{-1}$ with a median error bar of 0.9 $m\,s^{-1}$ (see Fig. 2). We employ RV-constant stars (rms < 10 $m\,s^{-1}$) to calculate NZPs, with the exact procedure being described in

Table 2. Nightly zero points for CARMENES.

JD	NZP (m s^{-1})	σ_{NZP} (m s^{-1})	N_{RV}	Flag
2457390	−6.35	1.23	0	1
2457391	−8.06	2.85	0	1
2457392	−9.04	3.25	1	1
2457393	−9.04	3.24	0	1
2457394	−6.73	4.53	0	1
2457395	−5.57	0.56	34	0
2457396	−9.23	1.08	3	0
2457397	−13.18	0.80	31	0
2457398	−13.48	0.84	23	0
2457399	−6.73	4.09	0	1

Notes. Listed are the Julian date (valid from UT12:00 to UT12:00 next day), the velocity of the nightly zero point (NZP), its uncertainty estimate σ_{NZP}, the number of RV-quiet star RVs used to calculate the NZP and a quality flag (where 0 indicates no issue with the calculation and 1 means that the NZP could not be calculated, in which case the NZP is replaced by a moving NZP average from adjacent nights). This is a sample list. The full table can be downloaded from CDS.
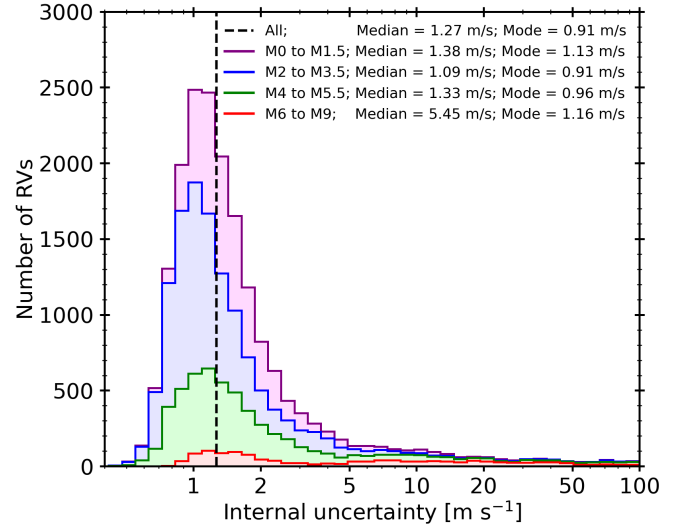

Fig. 3. Stacked histograms and statistical parameters (median and mode) of the internal precision (formal uncertainties) of the 18 642 precise RV measurements in the CARMENES DR1.

more detail by Trifonov et al. (2018). The resulting values are subsequently subtracted from each of the serval RV measurements. To avoid self-biasing the measurements, the zero point of RV-constant stars is calculated by removing the target itself from the calibration pool (Tal-Or et al. 2019). Tests revealed that NZP-corrected RVs improve the statistical significance of the best-fit models of CARMENES exoplanet discoveries, thus illustrating the benefits of the correction procedure. The same algorithm was applied by Tal-Or et al. (2019) to archival HIRES (High Resolution Echelle Spectrometer) Keck RVs and by Trifonov et al. (2020b) to reprocessed RVs from HARPS (High Accuracy Radial velocity Planet Searcher) spectra. In both cases the studies revealed and corrected systematic effects in those instruments.

Table 2 provides NZP values for all the CARMENES GTO nights. Reasons explaining the nightly offsets can be various, including a drift of the F-P, degraded quality of aged HCLs, strong instrument drifts during the ∼15 min calibration sequence (F-P and HCL calibration frames cannot be taken simultaneously), and different injection of calibration light coupled with insufficient scrambling. We were able to reduce some fraction of the night-to-night variability found during the initial CARMENES operations through hardware configuration changes and by employing a different strategy when acquiring the daily calibration sequences. As a result, the NZP scatter diminishes slightly after 2 yr of operation (Fig. 2). In addition to the night-to-night offsets, we also performed a correction for intra-night drift. The correction was found to be significant early in the survey and related to a temperature effect of the F-P subsystem. A hardware upgrade on 6 September 2017 (BJD 2458003) greatly decreased the temperature coupling and eliminated the need for such a correction. In any case, the effects of self-bias and intra-night drift correction are small. Further details on the instrument performance are provided in Bauer et al. (2020).

5. Results

The CARMENES DR1 provides raw spectroscopic data for the total sample of 362 targets but only full data products (including

RVs, spectroscopic indices, and CCF parameters) for 345 targets, that is, excluding 17 SB2 and ST3 systems. Precise RVs of the components of 12 of these spectroscopic multiple systems and full orbital and physical analyses were presented by Baroch et al. (2018, 2021). The remaining five binary systems, namely J05084−210, J06396−210, J09133+668, J16343+571 (CM Dra), and J23113+085, do not have a publication using CARMENES data yet. The procedure described in Sect. 4 was applied to the 18 642 suitable spectra and these produced the same number of RV determinations and associated data products. However, a fraction of those measurements lack a velocity drift calculation because of the poor quality of the simultaneous F-P spectrum. As a consequence, the number of drift-corrected RV measurements is 17 749, and these correspond to 344 targets. Only the faint target J16102−193 (K2−33) is not in the final sample because all spectra were taken without simultaneous F-P. All data products associated with the CARMENES DR1 and ancillary files are available online[7].

In Fig. 3, we illustrate the distribution of the formal uncertainties of the RV measurements (internal precision). Targets are grouped into four spectral-type bins using the same criteria as in Fig. 1. Brighter targets have typical uncertainties of ∼1 m s^{-1}, as their S/N at 1200 nm reached 150, but fainter targets have larger uncertainties due to the larger photon noise. The median value of the internal precision is 1.27 m s^{-1}, with the maximum of the distribution (mode) at 0.91 m s^{-1}.

The distribution of observations and their dispersion are illustrated in Fig. 4, also grouped in spectral-type bins. The scatter plot depicts the rms of the RV time series for each of the 344 NZP-corrected targets as a function of the number of observations, N_{obs}. Histograms of rms and number of observations are shown along both axes of the plot. The weighted rms of $n = 1 \dots N_k$ observations of each target k is calculated as

$$\text{rms} = \sqrt{\frac{1}{\sum_n w_n} \sum_n w_n (\text{RV}_n - \overline{\text{RV}})^2}, \tag{1}$$

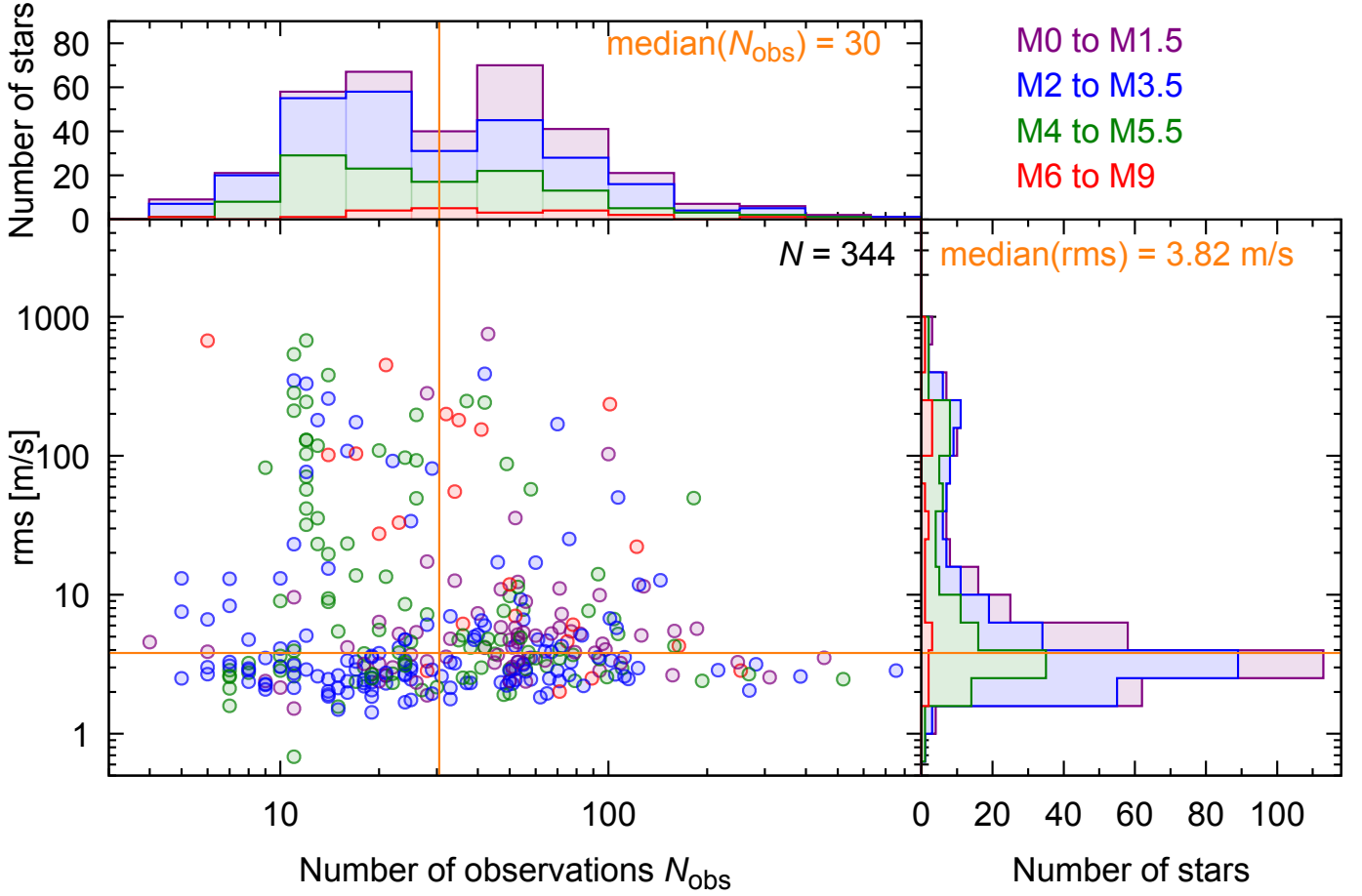[7] https://carmenes.cab.inta-csic.es

Fig. 4. Distribution of observations. The rms is computed for each of the 344 targets (circles colour-coded by spectral type) from their `serval` RV time series (NZP-corrected). No periodic signals (activity or planetary) were removed. The faint target J16102−193 (K2−33) is excluded, since all its spectra were taken without F-P.

where the epoch weights w_n include a jitter term σ_j, which is added in quadrature to the formal RV uncertainties $\sigma_{RV,n}$

$$w_n = \frac{1}{\sigma_{RV,n}^2 + \sigma_j^2}. \tag{2}$$

The σ_j and the re-weighted mean RVs were obtained self-consistently for each star via a maximum likelihood optimisation[8]. For the calculation we used the RVs as measured, with NZP correction, and no known signals of any nature (activity, planets) were subtracted. The median and mode of the distributions are 3.9 m s^{-1} and 3.3 m s^{-1}, respectively. These values can be compared to those characterising the internal precision in Fig. 3 to conclude that the RVs are most likely dominated by jitter (and signal) from astrophysical sources, which is statistically estimated to have a median contribution of ∼3.5 m s^{-1}. No obvious rms trends as a function of spectral type are observed except for a much higher rms (27.5 m s^{-1}) for the latest bin due to a large fraction of low S/N measurements.

5.1. High-resolution spectroscopic time series data

We compiled data tables of the time series of the RVs as described in Sect. 4, as well as additional ancillary parameters,

such as stellar activity indices, for each of the 345 M dwarfs (excluding SB2 and ST3) in the CARMENES sample. The dataset includes RV, CRX, dLW, and chromospheric line indices (Hα, Ca I, Ca II IRT, and Na I D) from `serval`, and the CCF RV, BIS, FWHM, and CON obtained with `raccoon`. Data from each spectral order are provided separately. For the RVs, both the values produced by `serval` (RVC) and those obtained after applying NZP corrections (AVC) are included. Furthermore, the exposure time and airmass of the observations, and the instrumental drift, the barycentric Earth RV, and the secular acceleration corrections applied to calculate RVCs are also provided.

Graphical representations of the time series of `serval` RVs corrected for NZPs as described in Sect. 4.4 have been produced for all targets with at least five valid NZP-corrected RV values and are available online[7]. An example is provided in Fig. 5 for the target J00051+457 (GJ 2). Periodogram analyses of the RVs and several relevant activity indices are also presented. Before computing the periodogram, we applied a clipping criterion to the measured values of the RVs and indices to avoid obvious outliers and poor-quality measurements. All data points deviating by more than 3σ from the mean were eliminated and so were measurements with error bars greater than the average value plus 3σ. Nightly averages were computed for the targets J00183+440 (GX And), J00184+440 (GQ And), and J07274+052 (Luyten's Star), as they had observations at higher cadence.

We subsequently computed the generalised Lomb-Scargle (GLS) periodogram (Zechmeister & Kürster 2009) of the RVs,
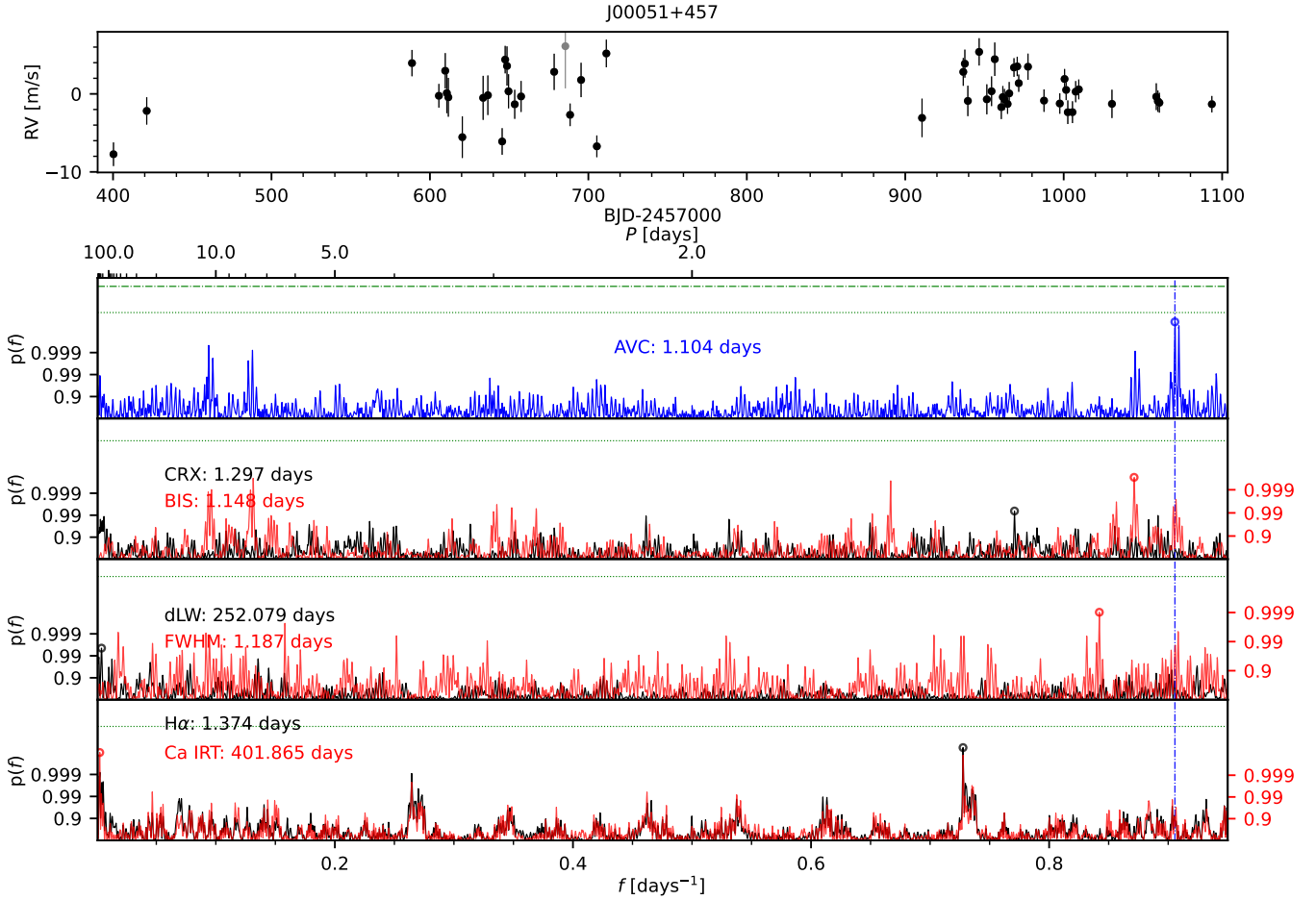
---
[8] See function `mlrms` in https://github.com/mzechmeister/python/blob/master/wstat.py

Fig. 5. Time series data and periodograms for target J00051+457 (GJ 2). *Top panel*: NZP-corrected RV time series. Outlier measurements (grey symbols; see text) are excluded in the periodogram calculation. *Bottom panels* (from top to bottom): GLS periodograms of the NZP-corrected RVs (AVC, blue), the chromatic index (CRX, black) and CCF bisector span (BIS, red), the differential line width (dLW, black) and the CCF FWHM (red), and the chromospheric activity indices corresponding to the Hα (black) and averaged Ca II IRT lines (red). The dash-dotted blue vertical line in all panels marks the position of the most significant peak in the RV periodogram, while the circles in the sub-panels highlight the position of the strongest signal in each periodogram, with the period given in the legend. The 0.1%, 1%, and 10% FAP levels are shown as horizontal dashed, dash-dotted, and dotted green lines, respectively, and are visible if they fall within the displayed vertical range. Vertical axes in panels that show two different datasets are scaled such that the FAP levels are identical. The colour code allows the graph to be related with the axis labels and legends.

the CRX, dLW, Hα, and Ca II IRT indices, and the CCF parameters BIS and FWHM. We grouped the indices and CCF parameters in pairs according to their expected sensitivity to the same activity phenomena, according to the analysis of Lafarga et al. (2021). Therefore, three panels with equivalent activity indicators are provided in Fig. 5, namely CRX & BIS, dLW & FWHM, and Hα & Ca II IRT. We considered periods ranging from twice the time span of the observations (to identify long-term variations) to the Nyquist frequency as computed from the closest RV measurement pairs of each dataset. However, an upper frequency limit of 0.95 day^{-1} was set to avoid daily aliases, except for targets with known short-period periodicities (close-in transiting planets and very fast-rotating stars). We calculated the false alarm probability (FAP) by running 10^5 bootstrap realisations of the datasets. From the bootstrapped data, we also computed the probability of each periodogram peak by assessing the number of times that the real periodogram at a given frequency is above all the realisations. This probability is related to the GLS power (Zechmeister et al. 2009) and is used in the graphical representation.

5.2. Exoplanets in the CARMENES GTO sample

The CARMENES sample was designed to preserve completeness as much as possible. Therefore, the initial target selection did not explicitly exclude known planet hosts. The inaugural CARMENES survey paper by Trifonov et al. (2018) analysed the CARMENES data for a sample of seven targets known to host 12 planets. In this study, a hitherto unknown second, long-period planet orbiting J11417+427 (GJ 1148) was reported, qualifying as the first exoplanet discovered by CARMENES. Shortly after, Reiners et al. (2018a) published the first exoplanet detected from data collected solely from the CARMENES survey. Since then, a succession of announcements has been made using data from the CARMENES blind survey, totalling 33 newly discovered planets in 28 planetary systems at the time of writing this paper. The new CARMENES planets are marked with a 'd' in column 'Type' of Table A.1. In some cases, CARMENES data were combined with precise RVs from other instruments (such as HARPS, HARPS-N, ESPRESSO, HIRES, IRD, MAROON-X, etc.) to enhance the statistical significance of the measurements.

Moreover, over the course of the survey, five already announced exoplanets were re-analysed using CARMENES data. Together with the 12 known planets in Trifonov et al. (2018), this makes up a total of 17 planets that are marked with an 'r' in Table A.1.

As explained in Sect. 1, the CARMENES Consortium decided to invest a fraction of the GTO time in following up on transiting planet candidates. Some of the targets came from the K2 mission (Howell et al. 2014), but most of them were provided by the ongoing TESS mission. The campaign has been fruitful, and CARMENES has led or contributed to the confirmation of 26 such planet candidates and helped measure their masses. The CARMENES planets resulting from follow-up activities are marked with an 'f' in Table A.1. The TESS planet candidate around J11044+304 (TOI-1806) has been followed up and validated with CARMENES; however, its parameters are not listed in the table because they are not yet sufficiently significant.

The columns in Table A.1 provide basic information on the targets and their planets. The parameters are taken from each of the quoted references. N_{CAR} and N_{other} are the number of RVs from CARMENES and other instruments, respectively, that were used in the corresponding publication. N_{CAR} may differ from the number of measurements in the DR1 release. Cases where N_{CAR} is greater than the number in DR1 correspond to recent publications that include observations taken after 31 December 2020, as part of the new CARMENES Legacy+ survey, while cases where N_{CAR} is below the number of measurements in DR1 are those where additional measurements within the CARMENES GTO were taken after the quoted publications. For four such planets we present new parameters in Table A.1 considering all the measurements in DR1. The four revised planets are J06548+332 b (GJ 251 b; Stock et al. 2020b) J08413+594 b,c (GJ 3512 b,c; Morales et al. 2019), and J16167+672S b (HD 147379 b; Reiners et al. 2018a).

In addition to the publications using CARMENES RVs, the DR1 includes measurements of targets for which there have been exoplanet detections or claims in the literature but do not have a specific publication using CARMENES data at the time of writing. These are listed in Table 3, along with the number of released CARMENES epochs. Besides planet detections and confirmations, there are some targets in our sample for which planets have been announced and are listed in exoplanet catalogues but could not be confirmed or are controversial given the data obtained with CARMENES or other instruments. The list of such planets is provided in Table 4. We are not including a planet around J00183+440 (GX And b) because the CARMENES observations now seem to support a planetary scenario for the 11.44-day signal (Trifonov et al., in prep.), in contrast to the initial CARMENES data (Trifonov et al. 2018), which were casting doubt on its nature.

Some of the challenged planets were already discussed in dedicated publications, as listed in Table 4. In two other cases, we carried out the analysis as part of the present work. Particularly, the candidates announced around J02222+478 (GJ 96) and J09561+627 (GJ 373) can be quite confidently ruled out as planets. For GJ 96, Hobson et al. (2018) announced a planet candidate based on 72 SOPHIE RVs[9]. The periodograms in Fig. 6 show that the 75-day signal present in SOPHIE data is absent in the 53 RVs from CARMENES. Instead, the dominant signal is at 28.5 days, which Hobson et al. (2018) already attributed to stellar activity. Indeed, this period is also present in the dLW, Ca II IRT, and Hα time series of the CARMENES data, thus ruling

Table 3. CARMENES survey targets with confirmed or claimed exoplanets that have no dedicated publications with CARMENES data.

Karmn	Star name	N_{CAR}	Ref.
J04219+213	LP 415-17 (K2-155)	4	Hir18
J04520+064	GJ 179	10	How10
J04538−177	GJ 180	25	Tuo14
J05019−069	LP 656-038	8	AD7
J06105−218	HD 42581 A	54	Tuo14
J07274+052	Luyten's Star	756	AD17
J08409−234	LP 844-008	27	AE12
J10023+480	BD+48 1829	23	Hob19
J11477+008	FI Vir	58	Bon18
J12388+116	GJ 480	7	Fen20
J13119+658	PM J13119+6550	12	Dem20
J16102−193	K2-33	27	Dav16
J16254+543	GJ 625	33	SM17
J16303−126	V2306 Oph	94	Wri16
J16581+257	BD+25 3173	55	Joh10
J17355+616	BD+61 1678C	26	Pin19
J17364+683	BD+68 946 AB	41	Bur14
J18353+457	BD+45 2743	16	GA21
J19206+731S	2MASS J19204172+7311434	22	Cad22
J22096−046	BD−05 5715	61	But06
J23064−050	TRAPPIST-1	17	Gil16

Notes. N_{CAR} is the number of measurements in CARMENES DR1.

References. AD17: Astudillo-Defru et al. (2017b), AE12: Anglada-Escudé et al. (2012), Bon18: Bonfils et al. (2018), Bur14: Burt et al. (2014), But06: Butler et al. (2006), Cad22: Cadieux et al. (2022), Dav16: David et al. (2016), Dem20: Demory et al. (2020), Fen20: Feng et al. (2020), GA21: González-Álvarez et al. (2021), Gil16: Gillon et al. (2016), Hir18: Hirano et al. (2018), Hob19: Hobson et al. (2019), How10: Howard et al. (2010), Joh10: Johnson et al. (2010), Pin19: Pinamonti et al. (2019), SM17: Suárez Mascareño et al. (2017), Tuo14: Tuomi et al. (2014), Wri16: Wright et al. (2016).

out its planetary nature. Phase-folded plots are shown in Fig. 7. The signal in GJ 373 at about 17.8 days announced as a planet by Tuomi et al. (2019) and Feng et al. (2020) can most definitely be attributed to stellar rotation modulation since it appears strongly in CARMENES activity indicators such as dLW and Hα and some CCF parameters, as can be seen in Fig. 8.

The sample of planets in Table A.1 is represented graphically in Fig. 9. Scatter plots combine the stellar mass, minimum planetary mass, orbital period, and RV semi-amplitude. The planet samples in the diagrams comprise those with CARMENES analyses (showing 'd', 'r', and 'f' separately in Table A.1) and those coming from the NASA Exoplanet Archive[10]. The latter correspond only to RV-detected planets (i.e. planets discovered through photometric transits are excluded). Also, histogram distributions of each of these quantities for the planets analysed with CARMENES data are depicted as side plots.

A few features in Fig. 9 are worth discussing. Regarding stellar mass, a majority of CARMENES planets have host stars with masses between $0.25\,M_\odot$ and $0.65\,M_\odot$, which constitute the bulk of the sample. Remarkably, half of the 24 RV planets with stellar hosts below $0.25\,M_\odot$ known to date have been discovered by CARMENES, a testament of the advantage offered by a

---

[9] The paper quotes 79 RVs, but only 72 RVs are published in https://cdsarc.cds.unistra.fr/ftp/J/A+A/618/A103/tablea1.dat

[10] https://exoplanetarchive.ipac.caltech.edu, accessed on 1 July 2022.

Table 4. Exoplanets challenged by CARMENES.

Karmn	Star name	Planet	P_p (days)	Ref.	Alternative	Ref.
J01125−169	YZ Cet	b	1.98	Ast17	2.02 d (alias)	Sto20a
J02002+130	TZ Ari	c	242	Fen20	Spurious	Qui22
J02222+478	GJ 96	b	73.9	Hob18	Spurious	This work
J04429+189	GJ 176	b	10.2	End08	Spurious, new 8.78 d	For09, But09, Tri18
J09561+627	GJ 373	b	17.8	Tuo19, Fen20	Rotation	This work
J10196+198	AD Leo	b	2.23	Tuo18	Rotation	Car20, Rob20, Kos22
J10564+070	CN Leo	c	2.69	Tuo19	Rotation	Laf21
J11033+359	Lalande 21185	b	9.9	But17	12.9 d	Dia19, Sto20b
J11302+076	K2-18	c	9.0	Clo17	Rotation	Sar18
J11509+483	GJ 1151	b	2.02	Mah21	390 d	Per21, Bla22
J16303−126	V2306 Oph	b	4.89	Wri16	1.27 d (alias)	Sab21

References. Ast17: Astudillo-Defru et al. (2017a); Bla22: Blanco-Pozo et al. (2023); But09: Butler et al. (2009); But17: Butler et al. (2017); Car20: Carleo et al. (2020); Clo17: Cloutier et al. (2017); Dia19: Díaz et al. (2019); End08: Endl et al. (2008); Fen20: Feng et al. (2020); For09: Forveille et al. (2009); Hob18: Hobson et al. (2018); Kos22: Kossakowski et al. (2022); Laf21: Lafarga et al. (2021); Mah21: Mahadevan et al. (2021); Per21: Perger et al. (2021); Qui22: Quirrenbach et al. (2022); Rob20: Robertson et al. (2020); Sab21: Sabotta et al. (2021); Sar18: Sarkis et al. (2018); Sto20a: Stock et al. (2020a); Sto20b: Stock et al. (2020b); Tri18: Trifonov et al. (2018); Tuo18: Tuomi et al. (2018); Tuo19: Tuomi et al. (2019); Wri16: Wright et al. (2016).
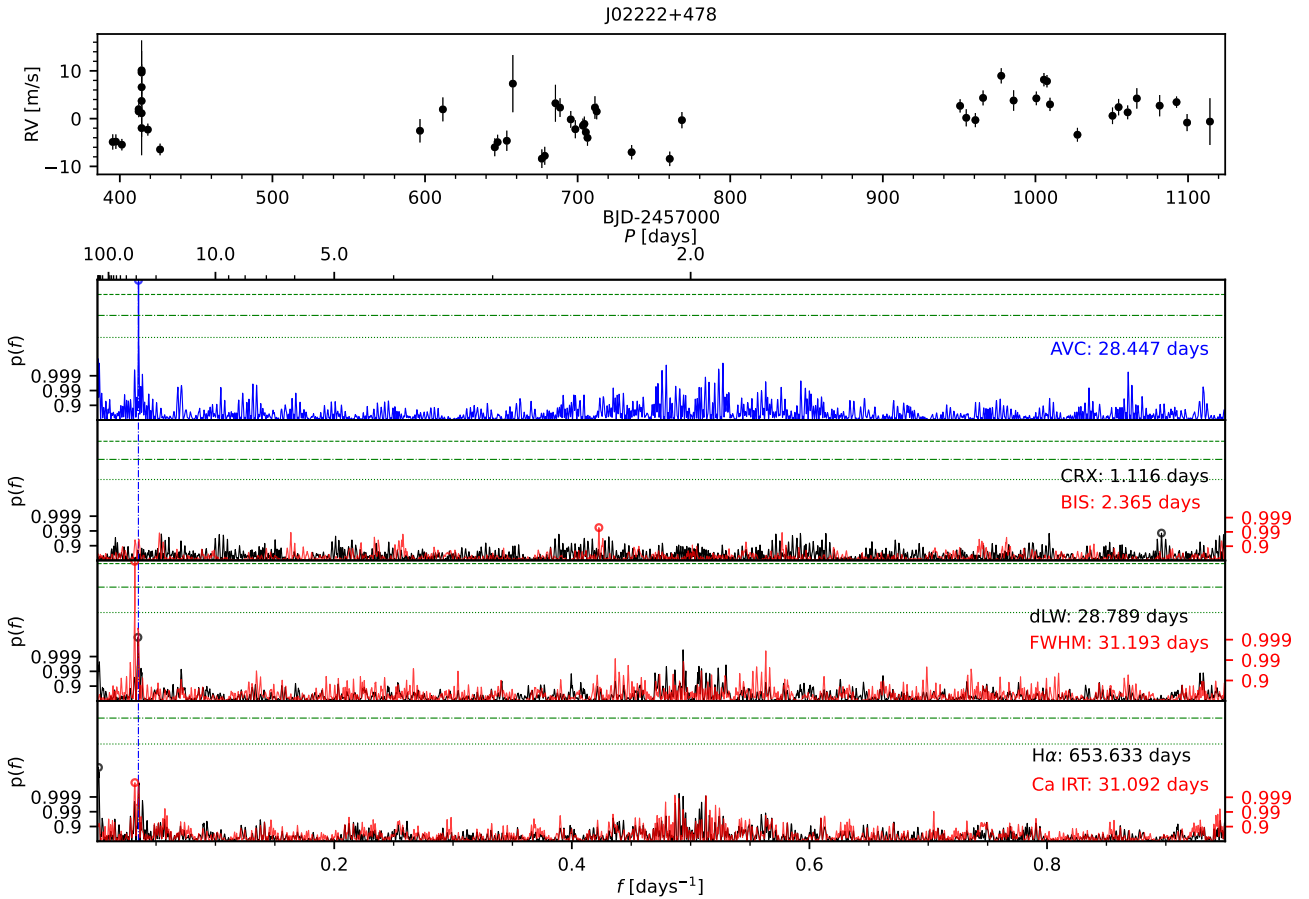

Fig. 6. Same as Fig. 5, but for J02222+478 (GJ 96). No planetary signal at a period of 73.9 days, as claimed by Hobson et al. (2018), is visible in the CARMENES data. The only significant periodicity is at ~28.5 days and seems to be related to activity given the counterparts in some of the indicators. Phase-folded plots are shown in Fig. 7.

red-optimised RV spectrometer in the late-type host regime. In terms of planetary mass, the majority of the CARMENES planets are in the super-Earth to the Neptune-mass domain, although several Earth-mass planets have been detected orbiting some of the lower-mass targets in our sample. Remarkable cases are two systems, J02530+168 (Teegarden's Star; Zechmeister et al. 2019) and J00067–075 (GJ 1002; Suárez Mascareño et al. 2023), each with two Earth-mass planets within the liquid-water habitable zones of their stars. Also, CARMENES has discovered six Saturn- and Jupiter-mass planets, some of them around very low-mass primaries, thus defying canonical planet formation models (Morales et al. 2019), which predict very low occurrence
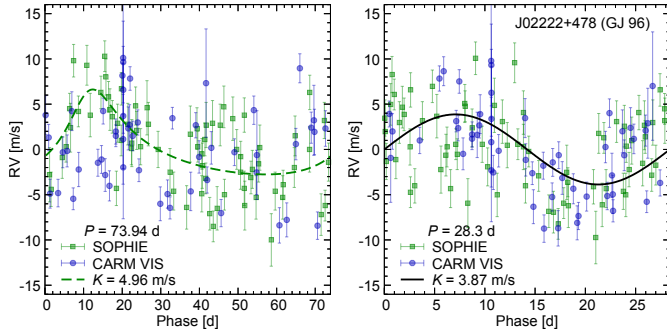
Fig. 7. Phase-folded RV data of J02222+478 (GJ 96). *Left*: SOPHIE (green squares) and CARMENES VIS (blue circles) phase-folded to a period of 73.94 days. The planetary Keplerian signal (dashed green line) proposed by Hobson et al. (2018) is based on the SOPHIE data alone and disfavoured by the CARMENES measurements. *Right*: same as the left panel, but phase-folded to the periodicity of 28.3 days, which is most likely associated with stellar activity.

rates of giant planets around M-type dwarfs (e.g. Schlecker et al. 2022). As expected for detectability reasons, most of the CARMENES planets have orbital periods from a few days to a few tens of days. Although not discussed here, the CARMENES GTO survey also announced (Baroch et al. 2021) two brown dwarf candidates on very long-period orbits ($P \gtrsim 3000$ days), around 10504+331 (GJ 3626) and J23556−061 (GJ 912).

5.3. Planet occurrence rates

Using the CARMENES DR1 sample we calculated planet occurrence rates in a similar way as was done by Sabotta et al. (2021, hereafter Sab21). In that work, preliminary occurrence statistics were calculated using a subsample of 71 targets having at least 50 CARMENES RV measurements. The re-analysis in the present work applies similar target selection criteria. From the initial 362 targets in the CARMENES GTO sample we excluded 124 targets because of several possible reasons: (i) they were added later for transit follow-up (mostly TESS candidates; 20 targets); (ii) they are spectroscopic binaries and triples (23 targets); (iii) they are part of the RV-loud sample as defined by Tal-Or et al. (2018) (52 targets); or (iv) we obtained fewer than ten RV measurements (29 targets). The sample therefore comprises a total of 238 targets, including 69 of the 71 targets in Sab21. For the two targets not included in the CARMENES DR1, one was excluded after being classified as a late-K dwarf (J18198−019, HD 168442), and the other one was subsequently classified as a resolved binary (J23113+085, NLTT 56083).

For the planetary sample, we re-ran the signal retrieval and vetting algorithm from Sab21 (see the results in Table A.2). The only change that we made was the period limit used for the long period planets. Sab21 included every signal if the time baseline was longer than two orbital periods, while here we include every signal with time coverage of at least 1.5 times the orbital period. If we considered the more conservative period limit of Sab21, we would exclude several giant planets from the planet sample and that would therefore reduce the statistical soundness of our analysis. As a result, we regard the new criterion as a better balance between being too conservative but still making sure that the signal is indeed periodic. Using this criterion, we identified 37 planets that can be confirmed with CARMENES data alone and three additional planet candidates (around J05033−173, J17033+514, and J18409−133). We also

include 13 planets with fewer than 50 RVs that were detected using data from other surveys (mainly HADES, HArps-n red Dwarf Exoplanet Survey, Pinamonti et al. 2022, and HARPS, Bonfils et al. 2013) if they induce an RV semi-amplitude of $K > 2$ m s^{-1}. We assume that we would have detected such planets if we had not terminated the observations because of our independent knowledge. We obtained those targets from a comparison with the two exoplanet databases on The Extrasolar Planets Encyclopaedia[11] (Schneider et al. 2011) and the NASA Exoplanet Archive[10]. In Table A.2, we mark planets that are listed in one of the databases and are well below our detection limits, planets with fewer than 50 RVs that are included in our planet sample, and archive planets that are not supported by CARMENES data. In this way we increase the planetary sample in Sab21 by 26 planets (from 27 to 53) for the recalculation of the occurrence rates. The total number of 53 planets reside in 43 planetary systems.

We calculated individual planet detection maps for all targets following the procedure described by Sab21. The numerical and graphical results are available online[7]. The global detection probabilities across the period-mass plane and the planets mentioned above are shown in Fig. 10, with the colour scale indicating the average of all detection probabilities for the individual grid points. There are five planets in a low-probability region, which means that we can only detect such planets for a small fraction of our sample. Unsurprisingly, these are Teegarden's Star b and c, YZ Cet c and d, and Wolf 1069 b, all of which are Earth-mass planets with very low-mass stellar hosts.

Using the same method as in Sab21, we obtained the power-law distribution in $M_{\rm pl} \sin i$ for the occurrence rate estimate (Fig. 6 in Sab21). The updated power-law with $N_{\rm pl, corrected} = a\,(M_{\rm pl} \sin i)^{\alpha}$ is only slightly shallower, with the slope changing from $\alpha = -1.14 \pm 0.16$ to $\alpha = -1.05 \pm 0.01$ for planets with masses below 30 $M_{\oplus}$, and from $\alpha = -0.26 \pm 0.17$ to $\alpha = -0.14 \pm 0.25$ for higher-mass planets (see Fig. 11). For our occurrence rate determination, we used this power-law as an initial assumption on the $M_{\rm pl} \sin i$ distribution, instead of assuming a log-uniform distribution[12]. The results are summarised in Table 5. We report both the number of planets per star ($\overline{n}_{\rm pl}$) and the frequency of stars with planets ($F_{\rm h}$). To obtain the latter, we repeated the analysis but instead of including all planets, we reduced the planet sample and took only the single planet with the highest K amplitude in the system. We then inspected the complete period-mass plane with periods of 1 day to 1000 days and $M_{\rm pl} \sin i$ of 1 $M_{\oplus}$ to 1 000 $M_{\oplus}$. In this parameter range, we determined an overall occurrence rate of $\overline{n}_{\rm pl} = 1.44 \pm 0.20$ planets per star and $F_{\rm h} = 94^{+4}_{-9}\%$ stars with planets. This means that the planet multiplicity in our sample is around 1.5 planets per system.

The analysis of Sab21 yielded occurrence rates that are larger by a factor of two for planets with 10 $M_{\oplus} < M_{\rm pl} \sin i < 100$ $M_{\oplus}$ and by 30% for the low-mass planets with 1 $M_{\oplus} < M_{\rm pl} \sin i < 10$ $M_{\oplus}$ with respect to the results obtained here for the full sample. The lower occurrence rates cannot be due to the looser requirement on orbital period coverage (1.5 instead of two orbital periods), since, if anything, this would result in larger occurrence rates. The smaller occurrence rates observed for the full CARMENES sample thus illustrate the effectiveness in terms of planet discovery of the pre-selection of targets that are observed

---

[11] http://exoplanet.eu
[12] The code and combined maps used to calculate occurrence rates are found in https://github.com/ssabotta/calculate_occurrence_rate
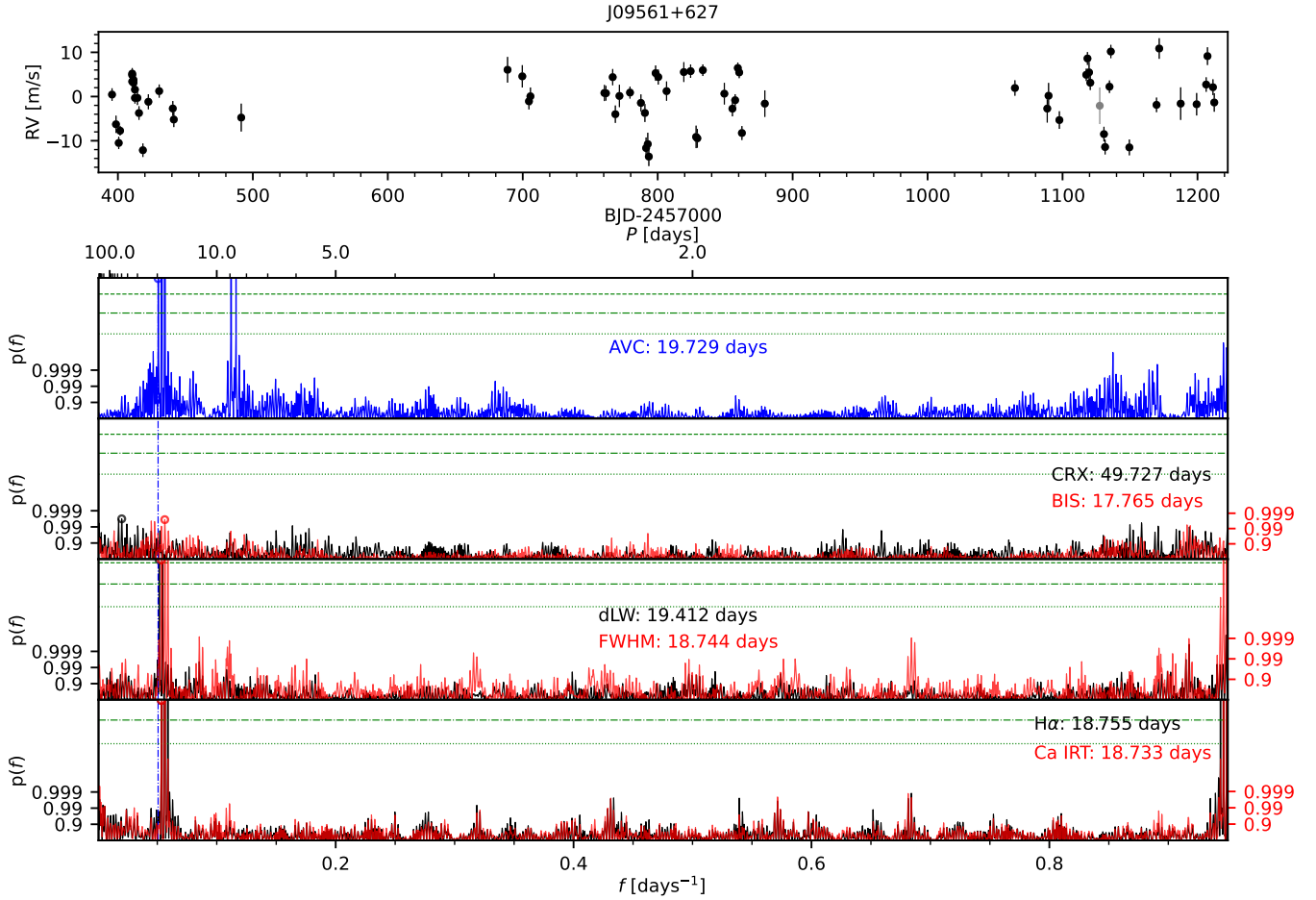
Fig. 8. Same as Fig. 5, but for J09561+627 (GJ 373). The periodic signal at 17.8 days attributed to a planet by Tuomi et al. (2019) and Feng et al. (2020) most likely arises from stellar activity in view of the counterparts in most of the activity indicators.

more intensively than others. Human intervention bias in this case leads to an over-estimation of occurrence rates. The survey sensitivity is higher for stars with planets because targets showing interesting signals that could be of planetary nature were observed more intensively. Sab21 pointed out this effect, and explicitly introduced the bias by rejecting all targets with fewer than 50 RVs, but it affects all targeted surveys that change the observing strategy based on acquired knowledge. In fact, by aiming at a specific number of observations for all of our targets, we minimised this effect. In the CARMENES DR1, we reach this number of 50 RVs for 42% of our targets, which corresponds to 112 stars. We are continuing the survey as part of the CARMENES Legacy+ programme. Even if the planet detection efficiency may not be as high as in the early stages of the GTO, the statistical value of the sample will greatly increase.

We compare our low-mass planet occurrence rates around M dwarfs to those of other surveys in Fig. 12. Our updated occurrence rates are consistent with the values obtained from the HARPS (Bonfils et al. 2013) and HADES (Pinamonti et al. 2022) surveys, but our results are based on a significantly larger statistical sample. The agreement is good despite the fact that both estimates by Bonfils et al. (2013) and Pinamonti et al. (2022) assumed a log-uniform distribution in planet mass, as opposed to our power-law relationship. If we also utilised a uniform distribution for our occurrence rate calculation, we would have obtained a lower occurrence rate of $0.58^{+0.11}_{-0.09}$ low-mass planets per star in orbits of up to 100 days (indicated as the grey square in Fig. 12).

In this parameter range, we obtained instead 1.06 ± 0.17 planets per star assuming a power-law distribution in $M_{pl} \sin i$. The difference occurs only in those regions of the period-mass plane with a strong sensitivity gradient, that is, below 10 $M_{\oplus}$. For higher planet masses, the choice of distribution does not affect our results significantly.

The comparison to transit surveys is not as straightforward due to the lack of an exact correspondence between the observed parameters. The expected value of $\sin i$ assuming randomly oriented orbits is ~0.8 (e.g. Hatzes 2019) and, therefore, our $M_{pl} \sin i$ bin of 1–10 $M_{\oplus}$ on average corresponds to a bin of 1.25–12.5 $M_{\oplus}$ in true M_{pl}. In this mass regime, planets could be rocky, water worlds, or puffy sub-Neptunes with very different densities (Luque & Pallé 2022). According to the mass-radius relation of Kanodia et al. (2019), this mass interval corresponds on average to the R_{pl} interval of 1.3–3.7 $R_{\oplus}$. In log-space this is only 75% of the radius interval of 1–4 $R_{\oplus}$ that Sab21 used for comparison with transiting planet statistics. Thus, in Fig. 12, we plot lower occurrence rates for the transit surveys (75% of those in Sab21). In any case, all occurrence rate estimates agree within a factor of two despite all the involved assumptions and the fact that we infer the occurrence rates from an overall detection sensitivity of 15% (considering the full period-mass plane).

The discussion above is relevant if one wants to find an absolute number of planets per star or to compare with transiting planet surveys or surveys targeting other stellar masses. Moreover, these calculations also serve as a valuable benchmark
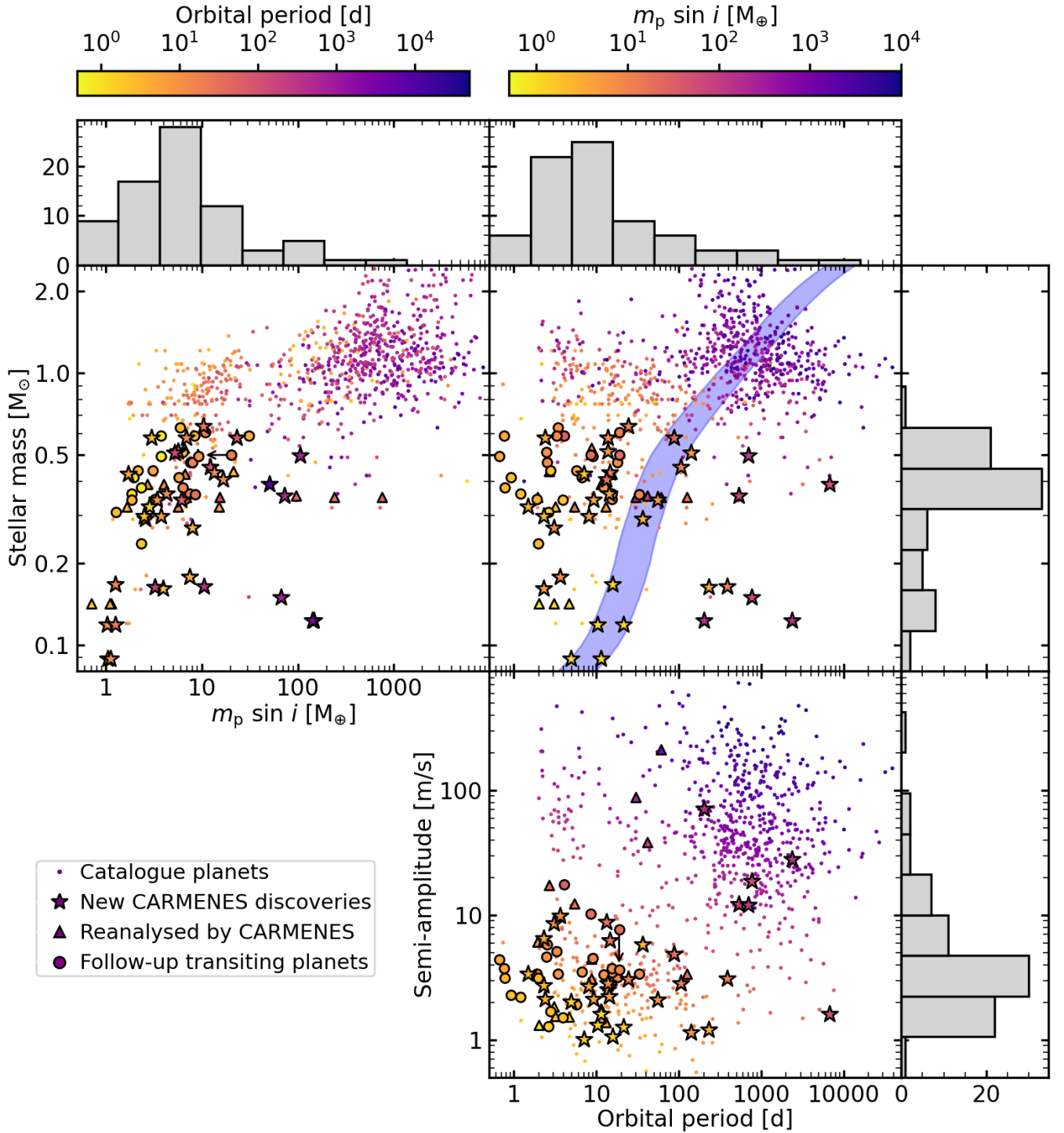
Fig. 9. Scatter plots of the CARMENES DR1 exoplanet sample compared to the complete sample of catalogued planets in the NASA Exoplanet Archive detected via RVs (903; small dots). Different symbols indicate planets newly detected from the CARMENES blind survey (33; stars), planets confirmed from transit follow-up (26; circles), and known planets re-analysed with CARMENES data (17; triangles). The three panels correspond to pairs of different relevant parameters, with the complementary colour scale introducing a third dimension. The histograms along the axes show distributions of the corresponding parameters for the CARMENES planet sample. The blue shaded band in the top-right panel represents the liquid-water habitable zone with limits defined by the 'runaway greenhouse' and 'maximum greenhouse' criteria (Kopparapu et al. 2013).

for planet formation theories that aim to reproduce population-level trends of exoplanets (e.g. Ida & Lin 2004; Bitsch et al. 2015; Miguel et al. 2020; Izidoro et al. 2021; Schlecker et al. 2021a,b; Mishra et al. 2021). Using the results of Sab21 as input, Schlecker et al. (2022) compared a planet sample based on the HARPS and CARMENES M-dwarf surveys to a synthetic

population computed with the Bern model of planet formation (Mordasini et al. 2012; Emsenhuber et al. 2021; Burn et al. 2021) and found three main discrepancies.

The first one is the observational finding of an excess of giant planets around lower-mass stars compared to the theoretical prediction. The simulations do not produce any giant planets
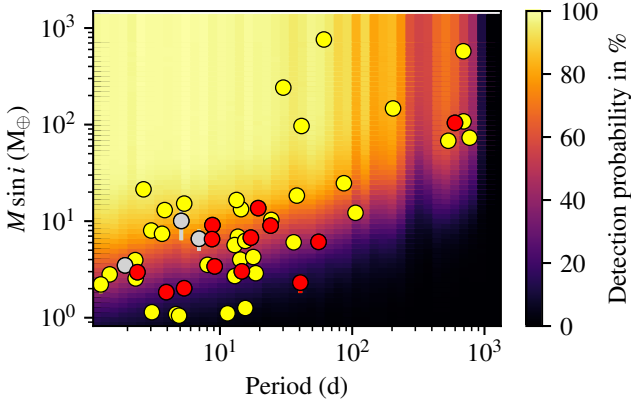
Fig. 10. CARMENES detection probability map in the period-mass plane derived from the observations of 238 targets. The detection probability is calculated using each target mass, and the average of all detection probabilities for the individual grid points is shown in the period-planet mass plane as a colour map. For example, a 10% detection probability for 238 targets indicates that the survey data can detect the respective planet in approximately 24 targets. Yellow circles indicate CARMENES planet detections and planet detections from other instruments that are confirmed by CARMENES data; grey circles planet candidates; and red circles planet detections from other surveys for which no sufficient CARMENES measurements are available to confirm them. The five planets in the low-probability detection region (<10%) are Teegarden's Star b and c, YZ Cet c and d, and Wolf 1069 b, all of which are Earth-mass planets with host stars of less than 0.2 $M_\odot$, thus suggesting that such planets are very abundant.
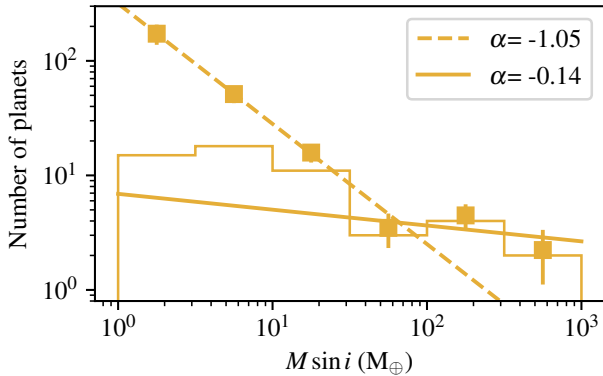

Fig. 11. Histogram of the number of planets detected in six $M_{pl} \sin i$ bins. The squares indicate the number of planets corrected for the survey sensitivity averaged over periods of up to 240 days. The dashed line and the solid line indicate the power law fit for $M_{pl} < 32\ M_\oplus$ and $M_{pl} > 32\ M_\oplus$, respectively.

around host stars with masses below 0.5 $M_\odot$. As was done by Sab21, we split the full CARMENES sample at a stellar mass of 0.337 $M_\odot$ and calculated giant planet occurrence rates. The median stellar masses of the two subsamples are 0.24 $M_\odot$ and 0.45 $M_\odot$. Using a strict limit for the giant planet mass of $M_{pl} > 100\ M_\oplus$, we obtained a rate of $0.021^{+0.018}_{-0.011}$ planets per star and $0.045^{+0.021}_{-0.016}$ planets per star for the low-mass and the high-mass stellar subsamples, respectively. The resulting occurrence rate ratio, $f_{high-mass}/f_{low-mass} = 2.14$, is marginally consistent with the giant planet frequency as a function of stellar mass published by Ghezzi et al. (2018),

$$f(M_\star, [Fe/H]) = 0.085^{+0.008}_{-0.010} M_\star^{1.05^{+0.28}_{-0.24}} 10^{1.05^{+0.21}_{-0.17}[Fe/H]}, \qquad (3)$$

assuming similar stellar metallicities, [Fe/H], in both samples.

Table 5. Planet occurrence rates for a sample of 238 M dwarfs in the CARMENES DR1 sample, including candidates and planet detections from other surveys.

		P (d)		
	1–10	10–100	100–1000	1–1000
(a) Planets with $100\ M_\oplus \sin i < M_{pl} < 1000\ M_\oplus$				
$N_{pl,det}$	0	2	4	6
$\bar{n}_{pl}$	<0.006	$0.010^{+0.010}_{-0.005}$	$0.03^{+0.01}_{-0.01}$	$0.03^{+0.02}_{-0.01}$
N_h	0	1	4	5
F_h	<0.006	$0.006^{+0.005}_{-0.005}$	$0.03^{+0.01}_{-0.01}$	$0.03^{+0.01}_{-0.01}$
(b) Planets with $10\ M_\oplus < M_{pl} \sin i < 100\ M_\oplus$				
$N_{pl,det}$	4	7	3	14
$\bar{n}_{pl}$	$0.02^{+0.02}_{-0.01}$	$0.04^{+0.02}_{-0.01}$	$0.04^{+0.02}_{-0.02}$	$0.09^{+0.03}_{-0.02}$
N_h	4	7	2	13
F_h	$0.02^{+0.02}_{-0.01}$	$0.04^{+0.02}_{-0.01}$	$0.03^{+0.02}_{-0.02}$	$0.09^{+0.02}_{-0.03}$
(c) Planets with $1\ M_\oplus < M_{pl} \sin i < 10\ M_\oplus$				
$N_{pl,det}$	18	15	0	33
$\bar{n}_{pl}$	$0.39^{+0.10}_{-0.07}$	$0.67^{+0.18}_{-0.15}$	< 0.40	$1.37^{+0.24}_{-0.24}$
N_h	15	10	0	25
F_h	$0.33^{+0.08}_{-0.07}$	$0.47^{+0.13}_{-0.13}$	< 0.40	$0.89^{+0.08}_{-0.11}$
(d) Planets with $1\ M_\oplus < M_{pl} \sin i < 1000\ M_\oplus$				
$N_{pl,det}$	22	24	7	53
$\bar{n}_{pl}$	$0.37^{+0.09}_{-0.07}$	$0.63^{+0.14}_{-0.12}$	$0.54^{+0.23}_{-0.17}$	$1.44^{+0.20}_{-0.20}$
N_h	19	18	6	43
F_h	$0.32^{+0.07}_{-0.07}$	$0.47^{+0.13}_{-0.09}$	$0.47^{+0.20}_{-0.16}$	$0.94^{+0.04}_{-0.09}$

Notes. $N_{pl,det}$: number of detected planets, $\bar{n}_{pl}$: average number of planets per star, N_h: number of planet host stars, F_h: frequency of stars with planets.

The second discrepancy between model and observation concerns the shape of the planet mass distribution. The distribution of $M_{pl} \sin i$ in the synthetic population is bimodal, whereas its counterpart in the observed sample is consistent with a power-law. In fact, our planet mass distribution does not deviate significantly from that in Sab21 (see Fig. 6 therein).

A third mismatch between the observed and model-predicted planet demographics as identified by Schlecker et al. (2022) is the orbital period distribution around stars with masses higher than 0.4 $M_\odot$. Short-period planets ($P_{orb} < 10$ days) are found to be significantly scarcer in the observed population compared to the synthetic one. The drop in occurrence rates at periods of less than 10 days, which was previously observed for stars with different stellar masses, does not hold for targets with masses below 0.4 $M_\odot$, with period distributions showing a good match. One possible explanation is a migration barrier having higher efficiency in protoplanetary disks around early M dwarfs that is not adequately accounted for by current models. For targets with $M < 0.337\ M_\odot$ we calculate $0.56^{+0.15}_{-0.14}$ and $0.63^{+0.23}_{-0.18}$ low-mass planets per star for the intervals 1–10 days and 10–100 days, respectively.

6. Conclusions

The CARMENES GTO survey ran from 1 January 2016 to 31 December 2020 and obtained 19 633 spectroscopic measurements of a sample of 362 targets. The sample was designed to be as complete as possible by including M dwarfs observable from
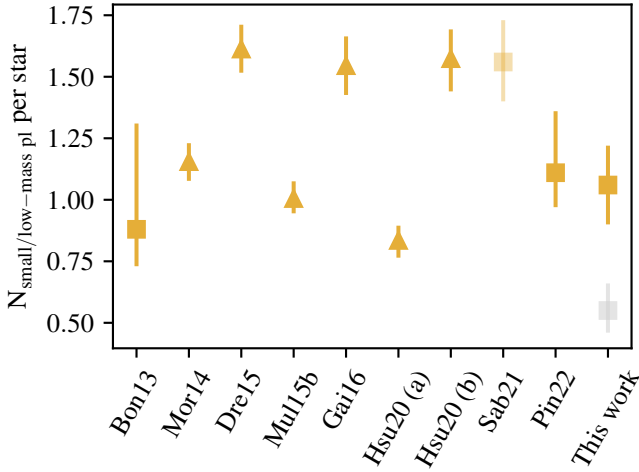
Fig. 12. Comparison of low-mass/small planet occurrence rates from various surveys (adapted from Sab21). The parameter range is 1 to 10 $M_\oplus$ in $M_{pl} \sin i$ for RV surveys and 1.3 to 3.7 $R_\oplus$ in R_{pl} for transit surveys. The error bars for transit surveys are Poisson errors based on the number of planet detections in the respective bins, and error bars from RV surveys are the 16% and 84% levels of the occurrence rate posterior distributions. Results using transiting planets from the *Kepler* mission are represented as triangles (Morton & Swift 2014; Dressing & Charbonneau 2015; Mulders et al. 2015; Gaidos et al. 2016; Hsu et al. 2020), and rates from the HARPS, HADES, and CARMENES RV surveys are represented as squares (Bonfils et al. 2013; Sabotta et al. 2021; Pinamonti et al. 2022, and this work). The grey square shows the occurrence rate from this work with the assumption of a log-uniform distribution in $M_{pl} \sin i$.

the Calar Alto Observatory with no selection criteria other than brightness limits and visual binarity restrictions. To best exploit the capabilities of the instrument, variable brightness cuts were applied as a function of spectral type to increase the presence of late-type targets. This effectively leads to a sample that does not deviate significantly from a volume-limited one for each spectral type. The global completeness of the sample is 15% of all known M dwarfs out to a distance of 20 pc and 48% at 10 pc.

The present paper accompanies the release of a large dataset, the CARMENES DR1. Raw data, pipeline-processed data, and high-level data products are provided, including 18 642 precise RVs for 345 targets (removing double- and triple-line systems). After correction of a NZP offset, the median internal precision of early and intermediate M-dwarf types is $\sim$1.2 m s^{-1}. This value increases to $\sim$5.4 m s^{-1} for late M spectral types due to their intrinsic faintness. The median rms of the RV time series of all the targets in the sample is calculated to be $\sim$3.9 m s^{-1}, where no signal has been subtracted. A comparison between the internal and external precisions indicates that the RV variance has a contribution of $\sim$3.5 m s^{-1} on top of the instrument error when treated as uncorrelated random noise. This external noise component is unlikely to be of instrumental origin. It is instead believed to arise from astrophysical effects, including Keplerian signals from planets but, most importantly, RV variability arising from stellar activity (e.g. active region rotation and evolution).

The CARMENES time series data have been analysed in the search for RV signals of a planetary nature. So far we have identified 33 new planets from the blind survey observations, which are complemented by 17 planets that we have re-analysed with CARMENES data and 26 planets from transit search space missions that we have confirmed and measured. The number of blind survey planets is in good agreement with the initial

estimates considering the properties of the stellar sample, the survey design, and the assumed planet occurrence rates (Garcia-Piquer et al. 2017). The new planets cover a broad region of the parameter space in terms of stellar host mass, planetary mass, and orbital period. A remarkable result is that CARMENES has discovered half of the RV planets known to orbit stars of masses below 0.25 $M_\odot$. This fact illustrates the prime 'hunting ground' of CARMENES thanks to the competitive advantage of the optimised red-sensitive design and the possibility of undertaking a massive survey with a large fraction of dedicated 4 m class telescope time over 5 yr.

With the CARMENES DR1 data, we have calculated new planet occurrence rates around M dwarfs to update the results already presented by Sab21. We have employed a subsample of 238 stars that fulfil a set of specific requirements. We still find a high long-period giant planet occurrence rate of around 3%, a high number of low-mass planets (1.06 planets per star in periods of 1 day to 100 days), and an overabundance of short-period planets around the lowest-mass stars of our sample compared to stars with higher masses. For our complete period-mass parameter space, we determine an overall occurrence rate of $\overline{n}_{pl} = 1.44 \pm 0.20$ planets per star and a fraction of $F_h = 94^{+4}_{-9}\%$ stars with planets. We calculate the overall CARMENES survey sensitivity to be 15% and find planets around 43 of 238 targets (i.e. 18% of the stars), which again shows that nearly every M dwarf hosts at least one planet.

In the present description of the CARMENES GTO data, we have focused on their use for precise RV work in the field of exoplanet detection and characterisation. Nevertheless, we have shown in a number of publications that these data are also of high value to a variety of science cases within stellar astrophysics, such as studying atmospheric parameters (T_{eff}, $\log g$, and chemical abundances; Passegger et al. 2018, 2019, 2020, 2022; Fuhrmeister et al. 2019a; Marfil et al. 2020, 2021; Abia et al. 2020; Shan et al. 2021), determining fundamental properties (M, R, and magnetic field; Schweitzer et al. 2019; Shulyak et al. 2019; Reiners et al. 2022), and analysing magnetic activity (Tal-Or et al. 2018; Fuhrmeister et al. 2018, 2019b, 2020, 2022; Schöfer et al. 2019; Hintz et al. 2019, 2020; Baroch et al. 2020; Lafarga et al. 2021; Jeffers et al. 2022). CARMENES VIS channel data have also proved useful in addressing the study of exoplanet atmospheres via transit transmission spectroscopy (Yan et al. 2019, 2021; Casasayas-Barris et al. 2020, 2021; Sánchez-López et al. 2020; Khalafinejad et al. 2021; Czesla et al. 2022) and the Rossiter-McLaughlin effect (Oshagh et al. 2020; Sedaghati et al. 2022).

The CARMENES GTO survey is now complete. In terms of exoplanet RV detection, the survey has provided about 60 planet discoveries and confirmations, some of which are of very high scientific relevance, and, as a sample, is of great statistical value, thus contributing to a complete census of the planetary population in the solar neighbourhood. The initial goals of the survey have therefore been fulfilled. The CARMENES sample continues to be observed within the CARMENES Legacy+ programme. The ultimate goal is to reach 50 measurements for all suitable targets (i.e. excluding multiples, RV-loud stars, etc.). The CARMENES Legacy+ extension of the survey is expected to run at least until the end of 2023 and, eventually, to lead to a second release of CARMENES survey data with 50 measurements or more for about 300 nearby M dwarfs. Through the present release and future additions, the CARMENES data will continue to yield new exoplanet discoveries and enable abundant studies in other domains within stellar astrophysics and exoplanetary science.

References

Abia, C., Tabernero, H. M., Korotin, S. A., et al. 2020, A&A, 642, A227

Affer, L., Micela, G., Damasso, M., et al. 2016, A&A, 593, A117

Alonso-Floriano, F. J., Morales, J. C., Caballero, J. A., et al. 2015, A&A, 577, A128

Amado, P. J., Bauer, F. F., Rodríguez López, C., et al. 2021, A&A, 650, A188

Anglada-Escudé, G., & Butler, R. P. 2012, ApJS, 200, 15

Anglada-Escudé, G., Boss, A. P., Weinberger, A. J., et al. 2012, ApJ, 746, 37

Astudillo-Defru, N., Díaz, R. F., Bonfils, X., et al. 2017a, A&A, 605, L11

Astudillo-Defru, N., Forveille, T., Bonfils, X., et al. 2017b, A&A, 602, A88

Baranne, A., Queloz, D., Mayor, M., et al. 1996, A&AS, 119, 373

Baroch, D., Morales, J. C., Ribas, I., et al. 2018, A&A, 619, A32

Baroch, D., Morales, J. C., Ribas, I., et al. 2020, A&A, 641, A69

Baroch, D., Morales, J. C., Ribas, I., et al. 2021, A&A, 653, A49

Bauer, F. F., Zechmeister, M., & Reiners, A. 2015, A&A, 581, A117

Bauer, F. F., Zechmeister, M., Kaminski, A., et al. 2020, A&A, 640, A50

Bayliss, D., Gillen, E., Eigmüller, P., et al. 2018, MNRAS, 475, 4467

Bitsch, B., Lambrechts, M., & Johansen, A. 2015, A&A, 582, A112

Blanco-Pozo, J., Perger, M., Damasso, M., et al. 2023, A&A, in press, https://doi.org/10.1051/0004-6361/202245053

Bluhm, P., Luque, R., Espinoza, N., et al. 2020, A&A, 639, A132

Bluhm, P., Pallé, E., Molaverdikhani, K., et al. 2021, A&A, 650, A78

Bonfils, X., Forveille, T., Delfosse, X., et al. 2005, A&A, 443, L15

Bonfils, X., Lo Curto, G., Correia, A. C. M., et al. 2013, A&A, 556, A110

Bonfils, X., Astudillo-Defru, N., Díaz, R., et al. 2018, A&A, 613, A25

Burn, R., Schlecker, M., Mordasini, C., et al. 2021, A&A, 656, A72

Burt, J., Vogt, S. S., Butler, R. P., et al. 2014, ApJ, 789, 114

Butler, R. P., Johnson, J. A., Marcy, G. W., et al. 2006, PASP, 118, 1685

Butler, R. P., Howard, A. W., Vogt, S. S., & Wright, J. T. 2009, ApJ, 691, 1738

Butler, R. P., Vogt, S. S., Laughlin, G., et al. 2017, AJ, 153, 208

Caballero, J. A., Guàrdia, J., López del Fresno, M., et al. 2016, in Proc. SPIE, 9910, 99100E

Cadieux, C., Doyon, R., Plotnykov, M., et al. 2022, AJ, 164, 96

Cale, B. L., Reefe, M., Plavchan, P., et al. 2021, AJ, 162, 295

Carleo, I., Malavolta, L., Lanza, A. F., et al. 2020, A&A, 638, A5

Casasayas-Barris, N., Pallé, E., Yan, F., et al. 2020, A&A, 635, A206

Casasayas-Barris, N., Orell-Miquel, J., Stangret, M., et al. 2021, A&A, 654, A163

Chaturvedi, P., Bluhm, P., Nagel, E., et al. 2022, A&A, 666, A155

Cifuentes, C., Caballero, J. A., Cortés-Contreras, M., et al. 2020, A&A, 642, A115

Cloutier, R., Astudillo-Defru, N., Doyon, R., et al. 2017, A&A, 608, A35

Cortés-Contreras, M., Béjar, V. J. S., Caballero, J. A., et al. 2017, A&A, 597, A47

Czesla, S., Lampón, M., Sanz-Forcada, J., et al. 2022, A&A, 657, A6

Damasso, M., Perger, M., Almenara, J. M., et al. 2022, A&A, 666, A187

David, T. J., Hillenbrand, L. A., Petigura, E. A., et al. 2016, Nature, 534, 658

Delfosse, X., Forveille, T., Beuzit, J. L., et al. 1999, A&A, 344, 897

Demory, B. O., Pozuelos, F. J., Gómez Maqueo Chew, Y., et al. 2020, A&A, 642, A49

Díaz, R. F., Delfosse, X., Hobson, M. J., et al. 2019, A&A, 625, A17

Díez Alonso, E., Caballero, J. A., Montes, D., et al. 2019, A&A, 621, A126

Dreizler, S., Crossfield, I. J. M., Kossakowski, D., et al. 2020, A&A, 644, A127

Dressing, C. D., & Charbonneau, D. 2015, ApJ, 807, 45

Emsenhuber, A., Mordasini, C., Burn, R., et al. 2021, A&A, 656, A69

Endl, M., Cochran, W. D., Tull, R. G., & MacQueen, P. J. 2003, AJ, 126, 3099

Endl, M., Cochran, W. D., Wittenmyer, R. A., & Boss, A. P. 2008, ApJ, 673, 1165

Espinoza, N., Pallé, E., Kemmer, J., et al. 2022, AJ, 163, 133

Feng, F., Shectman, S. A., Clement, M. S., et al. 2020, ApJS, 250, 29

Forveille, T., Bonfils, X., Delfosse, X., et al. 2009, A&A, 493, 645

Fuhrmeister, B., Czesla, S., Schmitt, J. H. M. M., et al. 2018, A&A, 615, A14

Fuhrmeister, B., Czesla, S., Hildebrandt, L., et al. 2019a, A&A, 632, A24

Fuhrmeister, B., Czesla, S., Schmitt, J. H. M. M., et al. 2019b, A&A, 623, A24

Fuhrmeister, B., Czesla, S., Hildebrandt, L., et al. 2020, A&A, 640, A52

Fuhrmeister, B., Czesla, S., Nagel, E., et al. 2022, A&A, 657, A125

Gaia Collaboration (Smart, R. L., et al.) 2021, A&A, 649, A6

Gaidos, E., Mann, A. W., Kraus, A. L., & Ireland, M. 2016, MNRAS, 457, 2877

Garcia-Piquer, A., Morales, J. C., Ribas, I., et al. 2017, A&A, 604, A87

Ghezzi, L., Montet, B. T., & Johnson, J. A. 2018, ApJ, 860, 109

Gillon, M., Jehin, E., Lederer, S. M., et al. 2016, Nature, 533, 221

González-Álvarez, E., Zapatero Osorio, M. R., Caballero, J. A., et al. 2020, A&A, 637, A93

González-Álvarez, E., Petralia, A., Micela, G., et al. 2021, A&A, 649, A157

González-Álvarez, E., Zapatero Osorio, M. R., Sanz-Forcada, J., et al. 2022, A&A, 658, A138

Hatzes, A. P. 2019, The Doppler Method for the Detection of Exoplanets (IOP Publishing)

Hintz, D., Fuhrmeister, B., Czesla, S., et al. 2019, A&A, 623, A136

Hintz, D., Fuhrmeister, B., Czesla, S., et al. 2020, A&A, 638, A115

Hirano, T., Dai, F., Livingston, J. H., et al. 2018, AJ, 155, 124

Hobson, M. J., Díaz, R. F., Delfosse, X., et al. 2018, A&A, 618, A103

Hobson, M. J., Delfosse, X., Astudillo-Defru, N., et al. 2019, A&A, 625, A18

Howard, A. W., Johnson, J. A., Marcy, G. W., et al. 2010, ApJ, 721, 1467

Howell, S. B., Sobeck, C., Haas, M., et al. 2014, PASP, 126, 398

Hoyer, S., Gandolfi, D., Armstrong, D. J., et al. 2021, MNRAS, 505, 3361

Hsu, D. C., Ford, E. B., & Terrien, R. 2020, MNRAS, 498, 2249

Ida, S., & Lin, D. N. C. 2004, ApJ, 604, 388

Izidoro, A., Bitsch, B., Raymond, S. N., et al. 2021, A&A, 650, A152

Jeffers, S. V., Schöfer, P., Lamert, A., et al. 2018, A&A, 614, A76

Jeffers, S. V., Barnes, J. R., Schöfer, P., et al. 2022, A&A, 663, A27

Johnson, J. A., Howard, A. W., Marcy, G. W., et al. 2010, PASP, 122, 149

Kaminski, A., Trifonov, T., Caballero, J. A., et al. 2018, A&A, 618, A115

Kanodia, S., & Wright, J. 2018, RNAAS, 2, 4

Kanodia, S., Wolfgang, A., Stefánsson, G. K., Ning, B., & Mahadevan, S. 2019, ApJ, 882, 38

Kemmer, J., Stock, S., Kossakowski, D., et al. 2020, A&A, 642, A236

Kemmer, J., Dreizler, S., Kossakowski, D., et al. 2022, A&A, 659, A17

Khalafinejad, S., Molaverdikhani, K., Blecic, J., et al. 2021, A&A, 656, A142

Kopparapu, R. K., Ramirez, R., Kasting, J. F., et al. 2013, ApJ, 765, 131

Kossakowski, D., Kemmer, J., Bluhm, P., et al. 2021, A&A, 656, A124

Kossakowski, D., Kürster, M., Henning, T., et al. 2022, A&A, 666, A143

Kossakowski, D., Kürster, M., Trifonov, T., et al. 2023, A&A, 670, A84

Kürster, M., Endl, M., Rouesnel, F., et al. 2003, A&A, 403, 1077

Lafarga, M., Ribas, I., Lovis, C., et al. 2020, A&A, 636, A36

Lafarga, M., Ribas, I., Reiners, A., et al. 2021, A&A, 652, A28

Lalitha, S., Baroch, D., Morales, J. C., et al. 2019, A&A, 627, A116

Luque, R., & Pallé, E. 2022, Science, 377, 1211

Luque, R., Nowak, G., Pallé, E., et al. 2018, A&A, 620, A171

Luque, R., Pallé, E., Kossakowski, D., et al. 2019, A&A, 628, A39
Luque, R., Fulton, B. J., Kunimoto, M., et al. 2022, A&A, 664, A199
Mahadevan, S., Stefánsson, G., Robertson, P., et al. 2021, ApJ, 919, L9
Marfil, E., Tabernero, H. M., Montes, D., et al. 2020, MNRAS, 492, 5470
Marfil, E., Tabernero, H. M., Montes, D., et al. 2021, A&A, 656, A162
Miguel, Y., Cridland, A., Ormel, C. W., Fortney, J. J., & Ida, S. 2020, MNRAS, 491, 1998
Mishra, L., Alibert, Y., Leleu, A., et al. 2021, A&A, 656, A74
Morales, J. C., Mustill, A. J., Ribas, I., et al. 2019, Science, 365, 1441
Mordasini, C., Alibert, Y., Klahr, H., & Henning, T. 2012, A&A, 547, A111
Morton, T. D., & Swift, J. 2014, ApJ, 791, 10
Mulders, G. D., Pascucci, I., & Apai, D. 2015, ApJ, 814, 130
Nagel, E. 2019, PhD thesis, Universität Hamburg Germany, https://ediss.sub.uni-hamburg.de/handle/ediss/6280
Nagel, E., Czesla, S., Schmitt, J. H. M. M., et al. 2019, A&A, 622, A153
Nowak, G., Luque, R., Parviainen, H., et al. 2020, A&A, 642, A173
Nutzman, P., & Charbonneau, D. 2008, PASP, 120, 317
Oshagh, M., Bauer, F. F., Lafarga, M., et al. 2020, A&A, 643, A64
Pallé, E., Orell-Miquel, J., Brady, M., et al. 2023, A&A, submitted [arXiv:2301.06873]
Passegger, V. M., Reiners, A., Jeffers, S. V., et al. 2018, A&A, 615, A6
Passegger, V. M., Schweitzer, A., Shulyak, D., et al. 2019, A&A, 627, A161
Passegger, V. M., Bello-García, A., Ordieres-Meré, J., et al. 2020, A&A, 642, A22
Passegger, V. M., Bello-García, A., Ordieres-Meré, J., et al. 2022, A&A, 658, A194
Perdelwitz, V., Mittag, M., Tal-Or, L., et al. 2021, A&A, 652, A116
Perger, M., García-Piquer, A., Ribas, I., et al. 2017, A&A, 598, A26
Perger, M., Scandariato, G., Ribas, I., et al. 2019, A&A, 624, A123
Perger, M., Ribas, I., Anglada-Escudé, G., et al. 2021, A&A, 649, L12
Pinamonti, M., Sozzetti, A., Giacobbe, P., et al. 2019, A&A, 625, A126
Pinamonti, M., Sozzetti, A., Maldonado, J., et al. 2022, A&A, 664, A65
Piskunov, N. E., & Valenti, J. A. 2002, A&A, 385, 1095
Quirrenbach, A., Amado, P. J., Caballero, J. A., et al. 2014, in Proc. SPIE, 9147, 91471F
Quirrenbach, A., Amado, P. J., Caballero, J. A., et al. 2016, in Proc. SPIE, 9908, 990812
Quirrenbach, A., Passegger, V. M., Trifonov, T., et al. 2022, A&A, 663, A48
Reiners, A., & Zechmeister, M. 2020, ApJS, 247, 11
Reiners, A., Joshi, N., & Goldman, B. 2012, AJ, 143, 93
Reiners, A., Ribas, I., Zechmeister, M., et al. 2018a, A&A, 609, A5
Reiners, A., Zechmeister, M., Caballero, J. A., et al. 2018b, A&A, 612, A49
Reiners, A., Shulyak, D., Käpylä, P. J., et al. 2022, A&A, 662, A41
Reylé, C., Jardine, K., Fouqué, P., et al. 2021, A&A, 650, A201
Ribas, I., Tuomi, M., Reiners, A., et al. 2018, Nature, 563, 365
Ricker, G. R., Winn, J. N., Vanderspek, R., et al. 2015, J. Astron. Telescopes Instrum. Syst., 1, 014003
Robertson, P., Stefánsson, G., Mahadevan, S., et al. 2020, ApJ, 897, 125
Sabotta, S., Schlecker, M., Chaturvedi, P., et al. 2021, A&A, 653, A114
Sánchez-López, A., López-Puertas, M., Snellen, I. A. G., et al. 2020, A&A, 643, A24
Sarkis, P., Henning, T., Kürster, M., et al. 2018, AJ, 155, 257
Schlecker, M., Mordasini, C., Emsenhuber, A., et al. 2021a, A&A, 656, A71
Schlecker, M., Pham, D., Burn, R., et al. 2021b, A&A, 656, A73
Schlecker, M., Burn, R., Sabotta, S., et al. 2022, A&A, 664, A180
Schneider, J., Dedieu, C., Le Sidaner, P., Savalle, R., & Zolotukhin, I. 2011, A&A, 532, A79
Schöfer, P., Jeffers, S. V., Reiners, A., et al. 2019, A&A, 623, A44
Schweitzer, A., Passegger, V. M., Cifuentes, C., et al. 2019, A&A, 625, A68
Sedaghati, E., Sánchez-López, A., Czesla, S., et al. 2022, A&A, 659, A44
Seifahrt, A., Stürmer, J., Bean, J. L., & Schwab, C. 2018, SPIE Conf. Ser., 10702, 107026D
Seifert, W., Sánchez Carrasco, M. A., Xu, W., et al. 2012, SPIE Conf. Ser., 8446, 844633
Shan, Y., Reiners, A., Fabbian, D., et al. 2021, A&A, 654, A118
Shulyak, D., Reiners, A., Nagel, E., et al. 2019, A&A, 626, A86
Soto, M. G., Anglada-Escudé, G., Dreizler, S., et al. 2021, A&A, 649, A144
Stefánsson, G., Cañas, C., Wisniewski, J., et al. 2020, AJ, 159, 100
Stock, S., Kemmer, J., Reffert, S., et al. 2020a, A&A, 636, A119
Stock, S., Nagel, E., Kemmer, J., et al. 2020b, A&A, 643, A112
Stürmer, J., Stahl, O., Schwab, C., et al. 2014, SPIE Conf. Ser., 9151, 915152
Suárez Mascareño, A., González Hernández, J. I., Rebolo, R., et al. 2017, A&A, 605, A92
Suárez Mascareño, A., Rebolo, R., González Hernández, J. I., et al. 2018, A&A, 612, A89
Suárez Mascareño, A., González-Álvarez, E., Zapatero Osorio, M. R., et al. 2023, A&A, 670, A5
Tal-Or, L., Zechmeister, M., Reiners, A., et al. 2018, A&A, 614, A122
Tal-Or, L., Trifonov, T., Zucker, S., Mazeh, T., & Zechmeister, M. 2019, MNRAS, 484, L8
Toledo-Padrón, B., Suárez Mascareño, A., González Hernández, J. I., et al. 2021, A&A, 648, A20
Trifonov, T., Kürster, M., Zechmeister, M., et al. 2018, A&A, 609, A117
Trifonov, T., Lee, M. H., Kürster, M., et al. 2020a, A&A, 638, A16
Trifonov, T., Tal-Or, L., Zechmeister, M., et al. 2020b, A&A, 636, A74
Trifonov, T., Caballero, J. A., Morales, J. C., et al. 2021, Science, 371, 1038
Tuomi, M., Jones, H. R. A., Barnes, J. R., Anglada-Escudé, G., & Jenkins, J. S. 2014, MNRAS, 441, 1545
Tuomi, M., Jones, H. R. A., Barnes, J. R., et al. 2018, AJ, 155, 192
Tuomi, M., Jones, H. R. A., Butler, R. P., et al. 2019, AAS J., submitted [arXiv:1906.04644]
Turtelboom, E. V., Weiss, L. M., Dressing, C. D., et al. 2022, AJ, 163, 293
Wang, X.-Y., Rice, M., Wang, S., et al. 2022, ApJ, 926, L8
Wright, J. T., & Eastman, J. D. 2014, PASP, 126, 838
Wright, J. T., Marcy, G. W., Butler, R. P., & Vogt, S. S. 2004, ApJS, 152, 261
Wright, D. J., Wittenmyer, R. A., Tinney, C. G., Bentley, J. S., & Zhao, J. 2016, ApJ, 817, L20
Yan, F., Casasayas-Barris, N., Molaverdikhani, K., et al. 2019, A&A, 632, A69
Yan, F., Wyttenbach, A., Casasayas-Barris, N., et al. 2021, A&A, 645, A22
Zechmeister, M., & Kürster, M. 2009, A&A, 496, 577
Zechmeister, M., Kürster, M., & Endl, M. 2009, A&A, 505, 859
Zechmeister, M., Anglada-Escudé, G., & Reiners, A. 2014, A&A, 561, A59
Zechmeister, M., Reiners, A., Amado, P. J., et al. 2018, A&A, 609, A12
Zechmeister, M., Dreizler, S., Ribas, I., et al. 2019, A&A, 627, A49

[1] Institut de Ciències de l'Espai (ICE, CSIC), Campus UAB, c/ Can Magrans s/n, 08193 Bellaterra, Barcelona, Spain
e-mail: iribas@ice.cat
[2] Institut d'Estudis Espacials de Catalunya (IEEC), c/ Gran Capità 2–4, 08034 Barcelona, Spain
[3] Institut für Astrophysik und Geophysik, Georg-August-Universität, Friedrich-Hund-Platz 1, 37077 Göttingen, Germany
[4] Centro de Astrobiología (CAB), CSIC-INTA, Campus ESAC, Camino Bajo del Castillo s/n, 28692 Villanueva de la Cañada, Madrid, Spain
[5] Landessternwarte, Zentrum für Astronomie der Universität Heidelberg, Königstuhl 12, 69117 Heidelberg, Germany
[6] Thüringer Landessternwarte Tautenburg, Sternwarte 5, 07778 Tautenburg, Germany
[7] Instituto de Astrofísica de Andalucía (IAA-CSIC), Glorieta de la Astronomía s/n, 18008 Granada, Spain
[8] Centro Astronómico Hispano en Andalucía (CAHA), Observatorio de Calar Alto, Sierra de los Filabres, 04550 Gérgal, Almería, Spain
[9] Instituto de Astrofísica de Canarias (IAC), 38200 La Laguna, Tenerife, Spain
[10] Departamento de Astrofísica, Universidad de La Laguna, 38206 La Laguna, Tenerife, Spain
[11] Hamburger Sternwarte, Universität Hamburg, Gojenbergsweg 112, 21029 Hamburg, Germany
[12] Instituto Universitario de Ciencias y Tecnologías Espaciales de Asturias, c/ Independencia 13, 33004 Oviedo, Spain
[13] Departamento de Física de la Tierra y Astrofísica and IPARCOS-UCM (Instituto de Física de Partículas y del Cosmos de la UCM), Facultad de Ciencias Físicas, Universidad Complutense de Madrid, 28040 Madrid, Spain
[14] Space Telescope Science Institute, 3700 San Martin Drive, Baltimore, MD 21218, USA
[15] Department of Physics and Astronomy, Johns Hopkins University, Baltimore, MD 21218, USA
[16] Max-Planck-Institut für Astronomie, Königstuhl 17, 69117 Heidelberg, Germany
[17] Isdefe, Beatriz de Bobadilla 3, 28040 Madrid, Spain
[18] Centro de Astrobiología (CAB), CSIC-INTA, Carretera de Ajalvir km 4, E-28850 Torrejón de Ardoz, Madrid, Spain
[19] Lunar and Planetary Laboratory, University of Arizona, 1629 East University Boulevard, Tucson, AZ 85721, USA
[20] Max-Planck-Institut für Sonnensystemforschung, Justus-von-Liebig-Weg 3, 37077 Göttingen, Germany

[21] Centre for Exoplanets and Habitability and Department of Physics, University of Warwick, Coventry CV4 7AL, UK

[22] School of Physics and Astronomy, University of Birmingham, Edgbaston, Birmingham B15 2TT, UK

[23] Department of Astronomy and Astrophysics, University of Chicago, 5640 South Ellis Avenue, Chicago, IL 60637, USA

[24] Dipartimento di Fisica, Università degli Studi di Roma "Tor Vergata", Via della Ricerca Scientifica 1, 00133, Rome, Italy

[25] INAF – Osservatorio Astrofisico di Torino, via Osservatorio 20, 10025, Pino Torinese, Italy

[26] Consejo Superior de Investigaciones Científicas, Serrano 117, 28006 Madrid, Spain

[27] Universitäts-Sternwarte,Ludwig-Maximilians-UniversitätMünchen, Scheinerstrasse 1, 81679 München, Germany

[28] Exzellenzcluster Origins, Boltzmannstrasse 2, 85748 Garching, Germany

[29] Homer L. Dodge Department of Physics and Astronomy, University of Oklahoma, 440 West Brooks Street, Norman, OK 73019, USA

[30] Kimmel fellow, Helen Kimmel Center for Planetary Science, Weizmann Institute of Science, Rehovot, Israel

[31] Leiden Observatory, Leiden University, Postbus 9513, 2300 RA Leiden, The Netherlands

[32] Department of Astronomy/Steward Observatory, The University of Arizona, 933 North Cherry Avenue, Tucson, AZ 85721, USA

[33] Centre for Earth Evolution and Dynamics, Department of Geosciences, Universitetet i Oslo, Sem Sælands vei 2b, 0315 Oslo, Norway

[34] INAF – Osservatorio Astronomico di Padova, Vicolo dell' Osservatorio 5, 35122 Padova, Italy

[35] Department of Physics, Ariel University, Ariel 40700, Israel

[36] Departament of Astronomy, Sofijski universitet, Sv. Kliment Ohridski", 5 James Bourchier Boulevard, 1164 Sofia, Bulgaria

[37] AstroLAB IRIS, Provinciaal Domein "De Palingbeek", Verbrande-molenstraat 5, 8902 Zillebeke, Ieper, Belgium

[38] Vereniging Voor Sterrenkunde, Oude Bleken 12, 2400 Mol, Belgium

[39] Centre for Mathematical Plasma Astrophysics, Katholieke Universiteit Leuven, Celestijnenlaan 200B, bus 2400, 3001 Leuven, Belgium

[40] Department of Astronomy, University of Science and Technology of China, Hefei 230026, PR China

Appendix A: Additional tables

Table A.1. Exoplanets in the CARMENES survey target sample with publications using CARMENES data.

Karmn	Star name	N_{CAR}	N_{other}	$M_\star$ ($M_\odot$)	Pl.	K (m s^{-1})	$M_{\mathrm{pl}} \sin i$ ($M_\oplus$)	P_{pl} (d)	Type[a]	Ref.
J00067−075	GJ 1002	86	53	0.120	b	1.31 ± 0.14	1.08 ± 0.13	10.3465 ± 0.0025	d	SM22
					c	1.30 ± 0.14	1.36 ± 0.17	21.202 ± 0.013	d	SM22
J00183+440	GJ 15 A	208	297	0.391 ± 0.016	b	1.79 ± 0.24	$3.98^{+0.38}_{-0.29}$	11.436 ± 0.001	r	Tri22
					c	$1.62^{+0.57}_{-0.36}$	$50.4^{+6.9}_{-6.8}$	6694^{+164}_{-285}	d	Tri22
J00403+612	2MJ00402129+6112490	44	0	0.471 ± 0.011	b	$5.83^{+0.86}_{-0.91}$	$7.52^{+1.12}_{-1.38}$	2.527113 ± 0.000009	f	GA22b
					c	$3.19^{+1.16}_{-1.07}$	$7.94^{+2.88}_{-2.64}$	18.0881 ± 0.0002	f	GA22b
J01026+623	GJ 49	80	158	0.515 ± 0.019	b	2.52 ± 0.31	$5.63^{+0.67}_{-0.68}$	$13.8508^{+0.0053}_{-0.0051}$	d	Per19
J01066+192	LSPM J0106+1913	65	32	0.344 ± 0.005	b	$3.40^{+0.25}_{-0.30}$	3.21 ± 0.24	1.8805136 ± 0.0000025	f	Cha22
					c	$3.48^{+0.34}_{-0.35}$	$6.64^{+0.67}_{-0.68}$	15.532482 ± 0.000034	f	Cha22
J01125−169	YZ Cet	108	332	0.142 ± 0.010	b	$1.31^{+0.15}_{-0.15}$	$0.70^{+0.09}_{-0.08}$	$2.02087^{+0.00007}_{-0.00009}$	r	Sto20a
					c	$1.84^{+0.14}_{-0.14}$	$1.14^{+0.10}_{-0.10}$	3.0599 ± 0.0001	r	Sto20a
					d	$1.54^{+0.15}_{-0.15}$	1.09 ± 0.12	$4.65626^{+0.00028}_{-0.00029}$	r	Sto20a
J02002+130	TZ Ari	93	79	0.150 ± 0.010	b	$18.8^{+1.3}_{-1.2}$	67 ± 6	$771.4^{+1.3}_{-1.2}$	d	Qui22
J02489−145W	PMJ02489−1432W	33	0	0.512 ± 0.020	b	$4.65^{+0.60}_{-0.64}$	$6.28^{+0.84}_{-0.88}$	2.491986 ± 0.000003	f	Kos21
J02530+168	Teegarden's Star	238	0	0.089 ± 0.009	b	$2.02^{+0.19}_{-0.20}$	$1.05^{+0.13}_{-0.12}$	4.9100 ± 0.0014	d	Zec19
					c	1.61 ± 0.19	$1.11^{+0.16}_{-0.15}$	11.409 ± 0.009	d	Zec19
J02573+765	LHS 1478	57	13	0.236 ± 0.012	b	$3.13^{+0.23}_{-0.25}$	2.33 ± 0.20	1.949538 ± 0.000004	f	Sot21
J03133+047	CD Cet	106	0	0.161 ± 0.010	b	$6.51^{+0.22}_{-0.23}$	$3.95^{+0.42}_{-0.43}$	2.29070 ± 0.00012	d	Bau20
J04167−120	LP714-47	34	54	0.59 ± 0.02	b	17.6 ± 0.8	30.8 ± 1.5	4.052037 ± 0.000004	f	Dre20
J04343+430	2MJ04342248+4302148	55	0	0.495 ± 0.019	b	$4.41^{+0.73}_{-0.63}$	3.76 ± 0.63	$0.669140^{+0.000002}_{-0.000002}$	f	Blu21
					c	$4.53^{+1.01}_{-1.02}$	9.2 ± 2.1	$9.025^{+0.104}_{-0.119}$	f	Blu21
J04429+189	GJ 176	23	181	0.504 ± 0.013	b	$4.49^{+1.00}_{-0.23}$	$9.1^{+1.5}_{-0.7}$	$8.776^{+0.001}_{-0.002}$	r	Tri18
J06371+175	HD 260655	88	92	0.439 ± 0.011	b	1.69 ± 0.27	2.14 ± 0.34	2.76953 ± 0.00003	f	Luq22
					c	1.92 ± 0.30	3.09 ± 0.48	5.70588 ± 0.00007	f	Luq22
J06548+332	GJ 251	280	75	0.360 ± 0.015	b	2.24 ± 0.18	$4.27^{+0.37}_{-0.36}$	14.2383 ± 0.0018	d	Sto20b,TW
J08023+033	GJ 3473	64	88	0.360 ± 0.016	b	2.21 ± 0.35	$1.86^{+0.30}_{-0.30}$	1.198003 ± 0.000002	f	Kem20
					c	$3.75^{+0.45}_{-0.42}$	$7.41^{+0.91}_{-0.86}$	15.509 ± 0.033	f	Kem20
J08413+594	GJ 3512	182	0	0.123 ± 0.009	b	$71.23^{+0.32}_{-0.33}$	146 ± 7	203.13 ± 0.05	d	Mor19,TW
					c	27.9 ± 0.4	143 ± 7	2350^{+100}_{-80}	d	Mor19,TW
J09144+526	GJ 338 B	159	30	0.64 ± 0.07	b	3.07 ± 0.37	$10.27^{+1.47}_{-1.38}$	24.45 ± 0.02	d	GA20
J09360−216	GJ 357	10	128	0.342 ± 0.011	b	1.52 ± 0.25	1.84 ± 0.31	$3.93072^{+0.00008}_{-0.00006}$	f	Luq19
					c	2.13 ± 0.28	3.40 ± 0.46	$9.1247^{+0.0011}_{-0.0010}$	d	Luq19
					d	$2.09^{+0.34}_{-0.35}$	6.1 ± 1.0	55.661 ± 0.055	d	Luq19
J10088+692	TYC4384-1735-1	40	21	0.630 ± 0.024	b	$3.40^{+0.35}_{-0.34}$	$5.90^{+0.62}_{-0.61}$	$3.444717^{+0.000040}_{-0.000042}$	f	Blu20
J10185−117	LTT 3780	52	4	0.379 ± 0.016	b	$3.13^{+0.31}_{-0.31}$	$2.34^{+0.24}_{-0.23}$	0.768377 ± 0.000001	f	Now20
					c	$3.36^{+0.32}_{-0.31}$	$6.29^{+0.63}_{-0.61}$	$12.25213^{+0.00007}_{-0.00006}$	f	Now20
J10289+008	GJ 393	84	250	0.426 ± 0.017	b	1.01 ± 0.14	1.71 ± 0.24	$7.02679^{+0.00082}_{-0.00085}$	d	Ama21
J11033+359	Lalande 21185	321	416	0.390 ± 0.011	b	1.39 ± 0.14	2.69 ± 0.25	12.946 ± 0.005	r	Sto20b
J11302+076	K2-18	58	0	0.359 ± 0.047	b	$3.38^{+0.76}_{-0.75}$	$8.49^{+1.97}_{-2.08}$	32.9396 ± 0.00010	f	Sar18
J11417+427	GJ 1148	76	125	0.354 ± 0.015	b	$38.54^{+0.37}_{-0.37}$	$96.6^{+1.0}_{-1.3}$	$41.380^{+0.001}_{-0.002}$	r	Tri20

Table A.1. Continued.

Karmn	Star name	N_{CAR}	N_{other}	$M_\star$ ($M_\odot$)	Pl.	K (m s^{-1})	$M_{pl}\sin i$ ($M_\oplus$)	P_{pl} (d)	Type[a]	Ref.
J11421+267	Gl 436	113	525	0.436 ± 0.012	c	$12.26^{+0.59}_{-0.56}$	$72.1^{+3.2}_{-7.0}$	$532.6^{+1.0}_{-1.1}$	d	Tri20
					b	17.38 ± 0.17	$21.36^{+0.20}_{-0.21}$	$2.644^{+0.001}_{-0.001}$	r	Tri18
J11509+483	Gl 1151	97	71	0.164 ± 0.009	b	$3.10^{+0.38}_{-0.43}$	$10.6^{+1.3}_{-1.5}$	$389.7^{+5.4}_{-6.5}$	d	Bla22
J12123+544S	Gl 458 A	108	0	0.578 ± 0.021	b	$2.85^{+0.38}_{-0.39}$	$6.89^{+0.92}_{-0.95}$	$13.671^{+0.011}_{-0.010}$	d	Sto20b
J12479+097	Gl 486	76	65	0.323 ± 0.015	b	$3.370^{+0.078}_{-0.080}$	$2.82^{+0.11}_{-0.12}$	$1.467119^{+0.000031}_{-0.000030}$	d	Tri21
J13229+244	Gl 3779	104	0	0.27 ± 0.02	b	8.62 ± 0.39	8.0 ± 0.5	3.0232 ± 0.0004	d	Luq18
J13299+102	Gl 514	274	266	0.510 ± 0.051	b	$1.15^{+0.21}_{-0.19}$	5.2 ± 0.9	140.43 ± 0.41	d	Dam22
J13255+688	2MJ13253177+6850106	55	0	0.59 ± 0.02	b	$3.74^{+1.03}_{-0.99}$	$3.75^{+1.14}_{-1.88}$	$0.764597^{+0.000013}_{-0.000011}$	f	GA22a
					c	$5.10^{+1.02}_{-1.06}$	$8.32^{+1.90}_{-1.88}$	$3.294736^{+0.000034}_{-0.000036}$	f	GA22a
J14010-026	Gl 536	28	277	0.530 ± 0.011	b	$3.12^{+0.36}_{-0.19}$	$6.52^{+0.69}_{-0.40}$	$8.708^{+0.002}_{-0.001}$	r	Tri18
J14342-125	Gl 555	94	48	0.291 ± 0.014	b	5.46 ± 0.75	2.59 ± 0.34	$36.116^{+0.027}_{-0.029}$	d	GA22c
J15194-077	Gl 581	20	664	0.323 ± 0.013	b	$12.35^{+0.18}_{-0.20}$	$15.20^{+0.22}_{-0.27}$	$5.368^{+0.001}_{-0.001}$	r	Tri18
					c	$3.28^{+0.22}_{-0.22}$	$5.65^{+0.39}_{-0.39}$	$12.919^{+0.003}_{-0.002}$	r	Tri18
					e	$1.55^{+0.12}_{-0.13}$	$1.66^{+0.24}_{-0.16}$	$3.153^{+0.001}_{-0.006}$	r	Tri18
J15583+354	Gl 3929	73	0	0.309 ± 0.014	b	$1.29^{+0.47}_{-0.46}$	1.27 ± 0.46	$2.616267^{+0.000005}_{-0.000005}$	f	Kem22
J16167+672S	HD 147379	186	30	0.58 ± 0.08	b	$4.87^{+0.41}_{-0.37}$	$23.0^{+2.8}_{-2.9}$	86.57 ± 0.06	d	Rei18a,TW
J17378+185	Gl 686	100	198	0.426 ± 0.033	b	$3.02^{+0.18}_{-0.20}$	$6.64^{+0.53}_{-0.54}$	$15.5314^{+0.0015}_{-0.0014}$	r	Lal19
J17578+046	Barnard's Star	196	575	0.163 ± 0.022	b	1.20 ± 0.12	3.23 ± 0.44	$232.80^{+0.38}_{-0.41}$	d	Rib18
J18580+059	Gl 740	32	129	0.58 ± 0.06	b	$2.13^{+0.34}_{-0.32}$	$2.96^{+0.50}_{-0.48}$	$2.37756^{+0.00013}_{-0.00011}$	d	TP21
J19169+051N	HD 180617	123	296	0.45 ± 0.04	b	$2.85^{+0.16}_{-0.25}$	$12.2^{+1.0}_{-1.4}$	$105.90^{+0.09}_{-0.10}$	d	Kam18
J20260+585	Wolf 1069	268	0	0.167 ± 0.011	b	1.07 ± 0.17	1.26 ± 0.21	15.564 ± 0.015	d	Kos22b
J20450+444	Gl 806	67	160	0.413 ± 0.011	b	2.25 ± 0.20	1.90 ± 0.17	0.9263237 ± 0.0000009	f	Pal22
					c	3.55 ± 0.17	5.80 ± 0.30	6.64064 ± 0.00025	f	Pal22
J20451-313	AU Mic	100	310	0.50 ± 0.03	b	$10.23^{+0.88}_{-0.91}$	$20.12^{+1.72}_{-1.57}$	8.463000 ± 0.000002	f	Cal21
					c	< 7.7	< 20.1	18.859019 ± 0.000016	f	Cal21
J21164+025	LSPM J2116+0234	72	0	0.430 ± 0.031	b	$6.31^{+0.44}_{-0.43}$	13.4 ± 1.1	$14.4433^{+0.0079}_{-0.0086}$	d	Lal19
J21221+229	TYC 2187-512-1	94	0	0.498 ± 0.019	b	$12.02^{+0.47}_{-0.46}$	105 ± 6	$691.9^{+8.8}_{-8.6}$	d	Qui22
J21466+668	G264-012	159	0	0.297 ± 0.024	b	$2.72^{+0.28}_{-0.29}$	$2.50^{+0.29}_{-0.30}$	2.30538 ± 0.00031	d	Ama21
					c	$2.69^{+0.31}_{-0.30}$	$3.75^{+0.38}_{-0.47}$	8.0518 ± 0.0034	d	Ama21
J21474+627	TYC 4266-00736-1	57	0	0.606 ± 0.020	b	$3.64^{+0.50}_{-0.51}$	10.8 ± 1.5	18.85019 ± 0.00013	f	Esp22
J22137-176	Gl 1265	87	11	0.178 ± 0.018	b	$9.82^{+0.51}_{-0.52}$	7.4 ± 0.5	3.6511 ± 0.0001	d	Luq18
J22252+594	Gl 4276	100	0	0.406 ± 0.030	b	8.79 ± 0.27	$16.57^{+0.94}_{-0.95}$	13.352 ± 0.003	d	Nag19
J22532-142	Gl 876	28	594	0.350 ± 0.013	b	$212.07^{+0.27}_{-0.26}$	$760.9^{+1.0}_{-1.9}$	$61.082^{+0.006}_{-0.005}$	r	Tri18
					c	$88.34^{+0.25}_{-0.25}$	$241.5^{+0.7}_{-0.7}$	$30.126^{+0.011}_{-0.003}$	r	Tri18
					d	$6.14^{+0.25}_{-0.22}$	$6.91^{+0.22}_{-0.27}$	$1.938^{+0.001}_{-0.001}$	r	Tri18
					e	$3.39^{+0.35}_{-0.38}$	15.4 ± 1.3	$124.4^{+4.3}_{-4.7}$	r	Tri18

Notes. N_{CAR} is the number of CARMENES measurements used in the analysis to determine the listed parameters (i.e. it may not coincide with the number of measurements released as part of DR1). N_{other} is the number of measurements from other spectrographs used in the analysis. The stellar mass column, $M_\star$, lists the value used by the quoted publication and is consistent with the planet's minimum mass, $M_{pl}\sin i$. Small differences may exist with the values tabulated in Table 1.
$^{(a)}$d: Planet discovered by CARMENES; f: Transiting planet confirmed with CARMENES follow-up observations; r: Re-analysis with CARMENES data.

References. Ama21: Amado et al. (2021); Bau20: Bauer et al. (2020); Bla22: Blanco-Pozo et al. (2023); Blu20: Bluhm et al. (2020); Blu21: Bluhm et al. (2021); Cal21: Cale et al. (2021); Cha22: Chaturvedi et al. (2022); Dam22: Damasso et al. (2022); Dre20: Dreizler et al. (2020); Esp22: Espinoza et al. (2022); GA20: González-Álvarez et al. (2020); GA22a: González-Álvarez et al. (2022); GA22b: González-Álvarez et al. (in prep.); GA22c: González-Álvarez et al. (in prep.); Kam18: Kaminski et al. (2018); Kem20: Kemmer et al. (2020); Kem22: Kemmer et al. (2022); Kos21: Kossakowski et al. (2021); Kos22b: Kossakowski et al. (2023); Lal19: Lalitha et al. (2019); Luq18: Luque et al. (2018); Luq19: Luque et al. (2019); Luq22: Luque et al. (2022); Mor19: Morales et al. (2019); Nag19: Nagel et al. (2019); Now20: Nowak et al. (2020); Pal22: Pallé et al. (2023); Per19: Perger et al. (2019); Qui22: Quirrenbach et al. (2022); Rei18a: Reiners et al. (2018a); Rib18: Ribas et al. (2018); Sar18: Sarkis et al. (2018); Sot21: Soto et al. (2021); Sto20a: Stock et al. (2020a); Sto20b: Stock et al. (2020b); SM22: Suárez Mascareño et al. (2023); TP21: Toledo-Padrón et al. (2021); Tri18: Trifonov et al. (2018); Tri20: Trifonov et al. (2020a); Tri21: Trifonov et al. (2021); Tri22: Trifonov et al. (in prep.); TW: This work; Zec19: Zechmeister et al. (2019).

Table A.2. Periodic signals with FAP < 1% in the 238-target sample for occurrence rate analysis.

Karmn	P (d)	FAP	Remark
J00051+457			no signal
J00067−075			no signal
J00162+198E			no signal
J00183+440[a]	40.68	0.0912%	rotation
J00184+440	10136.69	< 10⁻⁶	$P > \frac{2}{3}$ time baseline
J00286−066			no signal
J00389+306	20.17	0.0203%	unsolved
J00570+450			no signal
J01013+613			no signal
J01025+716	43.53	< 10⁻⁶	dLW
J01026+623[a]	18.9	0.0359%	Hα
J01026+623[a]	9.35	0.0036%	rotation
J01048−181			no signal
J01125−169[a]	3.06	0.0108%	planet
J01125−169[a]	4.7	0.0346%	planet
J01125−169[a]	80.77	0.0004%	dLW
J01339−176			no signal
J01433+043			no signal
J01518+644			no signal
J02002+130	1.95	< 10⁻⁶	Hα, CRX, dLW
J02002+130	782.52	< 10⁻⁶	planet
J02015+637			no signal
J02070+496			no signal
J02123+035			no signal
J02222+478[d]	28.29	0.0048%	dLW
J02336+249			no signal
J02358+202			no signal
J02362+068			no signal
J02442+255			no signal
J02530+168	11.41	< 10⁻⁶	planet
J02530+168	174.09	< 10⁻⁶	CRX
J02530+168	4.91	< 10⁻⁶	planet
J02565+554W			no signal
J03133+047	2.29	< 10⁻⁶	planet
J03133+047	67.52	0.2525%	rotation
J03181+382			no signal
J03213+799			no signal
J03217−066			no signal
J03463+262			no signal
J03531+625			no signal
J04153−076	1.8	< 10⁻⁶	CRX
J04225+105			no signal
J04290+219	12.54	0.0036%	rotation
J04290+219	170.18	0.0489%	CRX
J04290+219	24.99	0.0326%	Hα, dLW
J04376−110			no signal
J04376+528	16.32	0.3865%	Hα, dLW
J04376+528	419.62	0.7739%	CaIRT
J04376+528	7.9	0.3618%	unsolved
J04429+189[c]			no signal
J04429+214			no signal
J04520+064[b]	10582.5	0.1972%	$P > \frac{2}{3}$ time baseline
J04538−177[a c]			no signal
J04588+498	8.89	0.0140%	unsolved
J05033−173	1.92	0.0015%	candidate
J05033−173	73.78	0.4055%	unsolved
J05127+196			no signal
J05280+096			no signal
J05314−036	1362.47	< 10⁻⁶	$P > \frac{2}{3}$ time baseline
J05314−036	34.09	0.0022%	Hα
J05348+138			no signal
J05360−076			no signal
J05365+113	11.76	< 10⁻⁶	Hα, dLW
J05365+113	12.45	0.0043%	Hα, dLW

Table A.2. Continued.

Karmn	P (d)	FAP	Remark
J05365+113	6.31	0.0836%	activity
J05366+112			no signal
J05415+534	9.03	0.0070%	CaIRT
J05421+124			no signal
J06011+595	44.0	0.0268%	dLW
J06011+595	82.97	0.0821%	dLW
J06024+498			no signal
J06103+821	409.8	0.0081%	CaIRT
J06105−218	2621.33	0.0001%	$P > \frac{2}{3}$ time baseline
J06371+175[a]			no signal
J06421+035			no signal
J06548+332	120.37	< 10⁻⁶	rotation
J06548+332	14.24	< 10⁻⁶	planet
J06548+332	53.65	0.0024%	rotation
J06594+193			no signal
J07033+346			no signal
J07044+682			no signal
J07274+052	19.62	0.0813%	planet
J07274+052	461.91	< 10⁻⁶	unsolved
J07274+052	95.0	< 10⁻⁶	rotation
J07287−032	616.27	0.5847%	unsolved
J07319+362N	4.78	0.6855%	unsolved
J07393+021	29.78	0.0121%	activity
J07403−174	6.61	0.1475%	unsolved
J07582+413			no signal
J08119+087			no signal
J08126−215			no signal
J08161+013	22.45	0.1773%	rotation
J08293+039			no signal
J08315+730			no signal
J08358+680	1.73	0.1084%	unsolved
J08409−234	710.89	< 10⁻⁶	planet
J08413+594	10118.37	< 10⁻⁶	$P > \frac{2}{3}$ time baseline
J08413+594	203.24	< 10⁻⁶	planet
J08413+594	2204.2	< 10⁻⁶	$P > \frac{2}{3}$ time baseline
J08526+283			no signal
J09028+680			no signal
J09143+526	1210.67	0.1987%	$P > \frac{2}{3}$ time baseline
J09143+526	16.28	< 10⁻⁶	Hα, dLW
J09144+526	16.66	< 10⁻⁶	Hα, dLW
J09144+526	24.43	0.0003%	planet
J09144+526	3971.21	< 10⁻⁶	$P > \frac{2}{3}$ time baseline
J09307+003	294.04	0.5392%	unsolved
J09360−216[c]			no signal
J09411+132			no signal
J09423+559			no signal
J09425+700	677.39	0.7290%	unsolved
J09428+700	2.48	0.0303%	Hα
J09447−182			no signal
J09468+760			no signal
J09511−123			no signal
J09561+627[d]	18.69	< 10⁻⁶	Hα, dLW
J10023+480	3.82	0.7102%	planet
J10122−037	10.66	0.0008%	rotation
J10122−037	21.43	0.0048%	Hα
J10167−119			no signal
J10196+198	2.24	< 10⁻⁶	CRX
J10251−102			no signal
J10289+008[a]	317.21	0.0051%	unsolved
J10350−094			no signal
J10482−113	1.52	0.0415%	dLW
J10482−113	2.93	0.1639%	rotation
J10508+068			no signal
J10564+070[d]	2.7	< 10⁻⁶	CRX, dLW
J10584−107	1.27	< 10⁻⁶	CRX

Table A.2. Continued.

Karmn	P (d)	FAP	Remark
J11000+228			no signal
J11026+219	13.76	0.0030%	CRX
J11026+219	13.93	0.2527%	CRX
J11033+359	12.94	$< 10^{-6}$	planet
J11033+359	2017.54	$< 10^{-6}$	$P > \frac{2}{3}$ time baseline
J11054+435	1026.37	0.0001%	$P > \frac{2}{3}$ time baseline
J11055+435			no signal
J11110+304W			no signal
J11126+189			no signal
J11306−080			no signal
J11417+427	45.9	$< 10^{-6}$	planet
J11417+427	639.31	$< 10^{-6}$	Hα
J11417+427	835.19	0.0736%	$P > \frac{2}{3}$ time baseline
J11421+267	2.64	$< 10^{-6}$	planet
J11467−140			no signal
J11476+786			no signal
J11477+008[a]			no signal
J11509+483	316.73	$< 10^{-6}$	rotation
J11511+352	11.12	0.0014%	rotation
J12100−150			no signal
J12111−199			no signal
J12123+544S	13.67	$< 10^{-6}$	planet
J12230+640	15.13	0.0005%	CRX
J12230+640	73.06	0.0586%	CRX
J12230+640	8254.83	$< 10^{-6}$	$P > \frac{2}{3}$ time baseline
J12248−182			no signal
J12312+086			no signal
J12373−208			no signal
J12479+097	1.42	$< 10^{-6}$	planet
J12479+097	650.94	0.3179%	unsolved
J13102+477			no signal
J13209+342	5962.88	$< 10^{-6}$	$P > \frac{2}{3}$ time baseline
J13229+244	3.02	$< 10^{-6}$	planet
J13229+244	87.79	0.0015%	Hα, CRX, dLW
J13299+102[a]	15.42	0.3861%	rotation
J13299+102[a]	15.83	0.0023%	rotation
J13299+102[a]	512.48	0.0589%	unsolved
J13427+332			no signal
J13450+176			no signal
J13457+148	105.98	0.0074%	rotation
J13457+148	306.51	0.0020%	unsolved
J13457+148	33.89	0.0007%	unsolved
J13458−179			no signal
J13582+125			no signal
J14010−026[c]			no signal
J14082+805			no signal
J14251+518			no signal
J14257+236E			no signal
J14257+236W	10002.44	0.2462%	$P > \frac{2}{3}$ time baseline
J14307−086	252.02	0.2434%	unsolved
J14342−125	113.37	$< 10^{-6}$	CaIRT
J14342−125	36.11	0.0015%	planet
J14524+123	26.71	0.0010%	rotation?
J14544+355			no signal
J15013+055			no signal
J15095+031			no signal
J15194−077	12.92	0.0148%	planet
J15194−077	5.37	$< 10^{-6}$	planet
J15598−082			no signal
J16028+205			no signal
J16167+672N	42.22	0.0208%	activity
J16167+672S	21.99	0.0641%	rotation
J16167+672S	365.13	$< 10^{-6}$	CaIRT, CRX
J16167+672S	86.43	$< 10^{-6}$	planet
J16254+543[a]			no signal

Table A.2. Continued.

Karmn	P (d)	FAP	Remark
J16303−126	1.26	0.3514%	planet
J16303−126	17.88	$< 10^{-6}$	planet
J16303−126	1.84	0.3134%	unsolved
J16327+126			no signal
J16462+164			no signal
J16554−083N			no signal
J16581+257	12.42	0.0500%	rotation
J16581+257[c]	661.35	0.0033%	$P > \frac{2}{3}$ time baseline
J17033+514	6.94	0.0752%	candidate
J17052−050			no signal
J17071+215			no signal
J17115+384	5.58	0.8902%	unsolved
J17166+080			no signal
J17198+417	23.13	0.3605%	unsolved
J17303+055			no signal
J17355+616[c]			no signal
J17364+683	38.56	$< 10^{-6}$	planet
J17378+185	15.52	0.0001%	planet
J17378+185	40.28	0.4268%	Hα, dLW
J17378+185	499.08	0.0479%	planet
J17542+073	1.55	0.2591%	activity
J17578+046[a]	287.23	0.0056%	rotation
J17578+046[a]	387.44	0.2243%	CaIRT, Hα, dLW
J17578+046[a]	652.12	0.0225%	unsolved
J17578+465			no signal
J18027+375			no signal
J18051−030			no signal
J18075−159			no signal
J18165+048	23239.74	0.0095%	$P > \frac{2}{3}$ time baseline
J18174+483	16.04	0.0332%	activity
J18174+483	7.96	0.4972%	CRX
J18180+387E			no signal
J18221+063			no signal
J18224+620	2.06	0.7429%	CaIRT
J18319+406	2.93	0.2034%	unsolved
J18346+401	5786.99	$< 10^{-6}$	$P > \frac{2}{3}$ time baseline
J18353+457[c]	2.62	0.0842%	Hα
J18363+136	8189.81	0.9454%	$P > \frac{2}{3}$ time baseline
J18409−133	5.1	0.2652%	candidate
J18419+318			no signal
J18427+596N	11.2	0.0018%	unsolved
J18427+596N	27647.04	$< 10^{-6}$	$P > \frac{2}{3}$ time baseline
J18427+596N	64.8	0.0871%	unsolved
J18427+596S	10000.0	$< 10^{-6}$	unsolved
J18427+596S	117.9	0.0053%	unsolved
J18427+596S	186.6	0.0209%	unsolved
J18480−145			no signal
J18482+076	1.4	0.8063%	rotation
J18498−238	1.43	0.0294%	CRX, dLW
J18498−238	2.89	$< 10^{-6}$	dLW
J18580+059[c]			no signal
J19070+208			no signal
J19072+208			no signal
J19084+322			no signal
J19098+176			no signal
J19169+051N[e]	132.39	$< 10^{-6}$	CRX
J19216+208			no signal
J19251+283			no signal
J19346+045	2.52	0.6353%	unsolved
J20260+585	16.21	0.0080%	planet
J20260+585	14.95	0.5846%	unsolved
J20260+585	403.71	$< 10^{-6}$	tellurics
J20305+654			no signal
J20336+617	175.74	0.6727%	CRX
J20405+154	153.66	0.7230%	unsolved

Table A.2. Continued.

Karmn	P (d)	FAP	Remark
J20450+444			no signal
J20525−169			no signal
J20533+621	118.6	0.7191%	CaIRT, CRX
J20556−140S			no signal
J20567−104	1.25	0.1960%	unsolved
J21019−063			no signal
J21152+257			no signal
J21164+025	14.46	$< 10^{-6}$	planet
J21164+025	43.71	0.0006%	Hα
J21221+229	39.91	0.0001%	Hα, dLW
J21221+229	686.81	$< 10^{-6}$	planet
J21348+515	26.33	0.7167%	rotation
J21463+382			no signal
J21466−001			no signal
J21466+668	2.31	$< 10^{-6}$	planet
J21466+668	8.05	0.0001%	planet
J21466+668	92.49	$< 10^{-6}$	rotation
J22021+014	10.95	0.0373%	Hα
J22057+656	122.52	$< 10^{-6}$	CRX
J22096−046^b	3998.46	$< 10^{-6}$	$P > \frac{2}{3}$ time baseline
J22114+409	15.22	0.5957%	rotation
J22115+184	374.96	$< 10^{-6}$	CRX
J22115+184	39.02	0.0015%	dLW
J22125+085	2911.44	$< 10^{-6}$	$P > \frac{2}{3}$ time baseline
J22137−176	3.65	$< 10^{-6}$	planet
J22137−176	588.11	$< 10^{-6}$	$P > \frac{2}{3}$ time baseline
J22231−176			no signal
J22252+594	13.35	$< 10^{-6}$	planet
J22298+414	5.78	0.0280%	dLW
J22330+093	34.06	0.6282%	unsolved
J22503−070			no signal
J22532−142	30.07	$< 10^{-6}$	planet
J22532−142	60.85	$< 10^{-6}$	planet
J22559+178			no signal
J22565+165	18.61	$< 10^{-6}$	rotation
J22565+165	1845.72	$< 10^{-6}$	$P > \frac{2}{3}$ time baseline
J22565+165	39.28	$< 10^{-6}$	Hα, dLW
J23216+172			no signal
J23245+578			no signal
J23340+001			no signal
J23351−023			no signal
J23381−162			no signal
J23419+441	175.09	0.0001%	unsolved
J23431+365			no signal
J23492+024	372.77	0.0001%	CaIRT
J23492+024	53.83	0.4878%	Hα
J23505−095			no signal

Notes. $^{(a)}$Targets with known planets below detection limit. $^{(b)}$Targets with long period planets. $^{(c)}$Targets with known planets that fall below the CARMENES detection limit but that are included in the analysis anyway (semi-amplitude $K > 2\,\mathrm{m\,s^{-1}}$ and $N_{\mathrm{AVC}} < 50$). $^{(d)}$Targets with claimed planets that are not supported by CARMENES data. $^{(e)}$Known planet host but at a different period.